Crack detection for dikes
using distributed temperature sensing

Simone de Roos

Delft University of Technology - Master Thesis

TU Delft

Crack detection for dikes

using distributed temperature sensing

by

Simone de Roos

Student number: 5187648
Project duration: February, 2022 – September, 2022
Thesis committee:

Dr. ir. J. P. Aguilar-López,	TU Delft (HE),	chairperson & daily supervisor
Dr. L. A. Duarte Campos,	TU Delft (HE),	supervisor
Dr. ir. P. J. Vardon,	TU Delft (GSE),	supervisor

TU Delft

Acknowledgements

Ten months ago, I stepped into the unknown by starting a research on crack detection for dikes using temperature data obtained with a fiber optic sensor, without any background in thermal systems. After a complete and explicit literature study and performing studies with a FEM program, this knowledge gap was filled and a crack detection method could be developed. Eventually, the link with peak-to-peak temperature amplitudes emerged to be useful.

Similarly to my research, my development could also be named peak-to-peak. The methodology itself turned out to be fairly straightforward, but small victories allowed me to push my limits and improve the research gradually, increasing progress and, with it, increasing my expertise in thermal processes and modeling with FEM.

This research would not have been possible without the support of many important people. I would like to thank my family and friends for supporting me during the struggles and progress of this research. You always showed interest in the topic, even tough I know you are not particularly interested in this research topic.

Also, a very special thanks to my roommates and fellow students for being a sparring partner when needed. You know how important this research has been to me and have fed me with ideas just at the right moments in time. In addition, you provided short moments of distraction on working days, which gave the perfect balance between research and relaxation.

I would like to express my sincere appreciation to my supervisors, Juan, Leo and Phil, who were my beacon at times when I got stuck and always kept me motivated, resulting in me getting the best out of myself and succeeding in research goals I never could dream of. The weekly meetings were a good incentive and, at the same time, I never felt suppressed due to your incredibly friendly, calm personalities. I experienced every meeting as an enjoyable get together and I have always felt that doing research together was a pleasant adventure.

Lastly I would like to thank the readers of this report for taking the time to read my research and interpret my findings. That means a lot to me.

'Dankjewel!'

Simone
September 19, 2022

Abstract

One-third of the Dutch dike system consists of peat dikes. Drought causes these dikes to crack and fail more easily. Visual dike inspections are therefore inefficient, especially considering the increasing climate changes of the future. Research has shown that a fiber optic sensor cable (FOS), used in distributed temperature sensing (DTS), can help measure soil thermal responses, but the question remains whether it is also suitable as a replacement for visual inspections of dikes. This study helps to answer this question by coupling a finite element method (FEM) model with measured DTS information collected at Flood Proof Holland (Delft). In addition, (thermal) images are used to calibrate the FEM model. The measurement period was 20 summer days. The measured data consisted of webcam images, thermal images, and temperature time series of a FOS cable. The meteorological data was obtained via a weather station located in Rotterdam. The FEM model, calibrated and validated with the measured data, helped to find the thermal response of the system in situations of which no data was available, for example having various crack dimensions, cable positions or climatic conditions. The more distinguished the material properties of air and soil are (days with high water content and/or high radiation), the better the crack detection via DTS. After correction for the overestimation influence of radiation on the black FOS cable on sunny afternoons, the thermal response of the crack is corresponding to the air temperature more compared to the thermal response of grass. Crack detection via DTS turned out to be possible by x,T- and t,T-plots (diurnal temperature variation) and a regression plot with the daily peak-to-peak amplitude of the air temperature on the one hand and the daily peak-to-peak amplitude of the cable on the other. The advantage of the regression plot is that only one DTS thermal time series is needed to determine if the segment is most likely cracked or not. Furthermore, the peak-to-peak axes allow for diurnal climatic condition indications, and with it the heat storage and release of the system: rainy, cloudy days are in lower axis regions whereas sunny, clear days are in higher axis regions. However, due to a small measurement period, this method is only fully proven for sunny afternoons. Future studies have to map the thermal processes for other situations too.

Keywords: desiccation crack detection, distributed temperature sensing, fiber optic sensor, FEM

Contents

List of Figures

List of Tables

List of Symbols

Derivatives in ODEs are expressed using d. Derivatives in PDEs are expressed using ∂.

$a[mm]$ = radius grass leave = $1mm$ [1]
$A[m^2]$ = surface
$b[cm]$ = distance between two grass leave centers = $3cm$ [1]
$B[-]$ = brightness of a (webcam) image
$C[Jkg^{-1}K^{-1}]$ = heat capacity
$C_a[Jkg^{-1}K^{-1}]$ = heat capacity air = $1000Jkg^{-1}K^{-1}$ (COMSOL)
$C_g[Jkg^{-1}K^{-1}]$ = heat capacity grass leaves = $3720Jkg^{-1}K^{-1}$ [2]
$C_w[Jkg^{-1}K^{-1}]$ = heat capacity water = $4200Jkg^{-1}K^{-1}$ (COMSOL)
$E[J]$ = energy
$F[-]$ = view factor = $0 < F \leq 1$
$F[kN]$ = force
$G[Wm^{-2}]$ = incoming irradiation
$h[Wm^{-2}K^{-1}]$ = heat transfer coefficient
$J[Wm^{-2}]$ = outgoing radiosity
$k[Wm^{-1}K^{-1}]$ = thermal conductivity
$k_a[Wm^{-1}K^{-1}]$ = thermal conductivity air = $0.025Wm^{-1}K^{-1}$ (COMSOL)
$k_g[Wm^{-1}K^{-1}]$ = thermal conductivity grass leaves = $1.10Wm^{-1}K^{-1}$ [3]
$k_w[Wm^{-1}K^{-1}]$ = thermal conductivity water = $0.58Wm^{-1}K^{-1}$ (COMSOL)
$m[kg]$ = mass
$mc[-]$ = moisture content = $\frac{\text{water mass}}{\text{solid mass}}$
$n[-]$ = refractive index
$n[-]$ = porosity
$n_p[-]$ = porosity peat = 0.9 [4]
$Nu[-]$ = Nusselt number
$p[Pa]$ = pressure
$q[Wm^{-2}]$ = heat flux
$Q[Wm^{-3}]$ = heat flux
$Re[-]$ = Reynolds number
$T[^\circ C$ or $K]$ = temperature
$x, y, z[-]$ = directions
$x[m]$ = distance
u or $U[ms^{-1}]$ = velocity
$V[m^3]$ = volume
$V_{tot}[m^3]$ = total volume peat soil = $9.2E^{-5}m^3$ (Equation 3.16)
$wc[-]$ = water content = $\frac{\text{water mass}}{\text{soil mass}}$ = $0 \leq wc \leq 1$
$\alpha[m^2s^{-1}]$ = thermal diffusivity
$\epsilon[-]$ = emissivity
$\mu[Pa \cdot s]$ = viscosity
$\rho[kgm^{-3}]$ = density
$\rho_a[kgm^{-3}]$ = density air = $1.2kgm^{-3}$
$\rho_g[kgm^{-3}]$ = density grass leaves = $200kgm^{-3}$ [5]
$\rho_{p,bulk}[kgm^{-3}]$ = bulk density peat = $1010kgm^{-3}$ [4]
$\rho_{p,dry}[kgm^{-3}]$ = density dry peat = $130kgm^{-3}$ [4]
$\rho_w[kgm^{-3}]$ = density water = $997kgm^{-3}$
$\sigma[Wm^{-2}K^{-4}]$ = Stefan-Boltzmann constant = $5.67 \times 10^{-8}Wm^{-2}K^{-4}$
$\Omega[-]$ = domain

List of Terms

A_{ptp} The peak-to-peak amplitude is the range between the minimum and maximum temperature measured in one day. 9, 28, 33

BDF Backward Differentiation Formula. 51

CABCRK Cable above crack point shown in Figure D.1. 3

CABGRS Cable above grass point shown in Figure D.1. 3

cable Cable on top of the soil, consisting of different layers including fiber. 11

cable-crack segment Amount of cable floating above the crack. 27, 32, 35

COMSOL The FEM model program. 15, 16, 23, 51

CRK Crack (bottom) point shown in Figure D.1. 3

DTS Distributed Temperature Sensing. 1, 2, 6, 7, 18, 21, 25, 29, 31–33, 35, 38, 55, 63

FEM Finite Element Method. ix, 1–3, 9, 11, 13, 15, 18, 21, 24, 28, 29, 31–35, 49, 63

fiber Fiber wires are present in the core of the cable, detecting differences in temperature. 11

FOS Fiber Optic Sensor cable, used in DTS. x, 1–3, 7, 11, 25, 28, 31, 33, 35, 37, 55

FPH Flood Proof Holland, the test site at which the desiccation crack in a peat dike is observed during the measuring period. 7, 14, 15, 27, 37

GRS Grass point shown in Figure D.1. 3

KNMI Koninklijk Nederlands Meteorologisch Instituut is the Dutch national weather service. ix, 7, 15, 33, 55

measuring period The period for which the data was collected: August 16, 2021 14:00 until September 6, 2021 8:00. 7

ODE Ordinary Differential Equation. xiii

PDE Partial Differential Equation. xiii, 49, 50

soil Water and solid particles together. 13

solid Solid particles only. 13

TRC Thermal Radiometric Camera. ix, 1, 3, 7, 21, 23–25, 29, 33, 35

Summary

Decades ago, scientists predicted a climate change so extreme that the way we live on earth had to be changed. Currently, the Earth already experiences more severe storms and long extreme dry spells, which will become even more frequent in the future. During a period of drought, dikes dry out and crack. When such a period is followed by lots of precipitation and water runoff, this leads to extremely dangerous stability situations. At this time, these desiccation cracks are only visually noticed by human dike inspections. This report describes a method that will allow the detection of cracks along the dike by means of a fiber optic cable. This distributed temperature sensing has already been discussed in several studies, but what is not discussed so far and what is done in this research, is link the measured DTS data with a FEM model in order to create a robust desiccation crack detection method.

The method consists of a regression plot that can identify cracks from data. The regression plot is based on several FEM studies. The basis of these studies lies in the original FEM model, which is a modeled fraction of peat soil covered with a grass canopy, cracked in the middle, and a fiber optic sensor cable on top. Model inputs are found using literature and field measurements on a cracked dike in Delft. The FEM model solves the temperature for all parts of the system using the heat balance equation that includes internal storage, conduction, radiation, and convection. Variations in crack shape, cable position, and ambient input data are also studied. Then all different 95% confidence intervals of all FEM studies performed are plotted into one regression plot, coupling the daily peak-to-peak amplitude of the environment temperature on the y axis with the daily peak-to-peak amplitude measured by the cable on the x axis. With this plot, it is possible to determine whether there is a cracked spot or not by only measuring the outside temperature and the cable temperature at the desired location.

The DTS data is a set of temperature time series of an existing crack and grass domain of a peat dike in Delft, obtained in the summer of 2021. Using the constructed FEM model, this DTS data set has been validated. The FEM model was calibrated with thermal images of the same cracked dike in Delft. Four points are investigated: the crack bottom (CRK), a point in the grass (GRS), a cable segment above the crack (CABCRK) and a cable segment above the grass (CABGRS). The thermal images show that the crack is colder than the grass during the day and warmer than the grass during the night ($A_{ptp,CRK} < A_{ptp,GRS}$). The DTS data show the reverse for the cable above the crack and grass ($A_{ptp,CABCRK} > A_{ptp,CABGRS}$). The FEM model was used to find which of these reflects reality.

One important influencing phenomenon turned out to be radiation and with it the embeddedness and shadyness of the cable. The system and the cable are heated by radiation, and the cable gives a biased overheated thermal time series since it is also heated up itself. This issue was improved by correcting the DTS data on this overheating. After filtering, the DTS data gave a response consistent with the thermal images ($A_{ptp,CABCRK} < A_{ptp,CABGRS}$). Therefore, in all probability, the reality turned out to be consistent with the TRC and the corrected DTS time series. In addition to radiation, the water content had a significant influence on the thermal response too. The robustness of the method in situations other than summer is unclear as data was only available for summer 2021. Furthermore, the (material) inputs of the FEM model are partly unconfirmed since the options found in literature vary widely and no material and soil moisture measurements of the dike were taken during the measurement period. The method works best in periods with high radiation and high water content, since then the regression lines of grass and crack are more distinguishable.

To conclude, the FEM model constructed in this research took away the uncertainty, regarding the measured DTS time series, by mapping the processes created by the conditions that affect the thermal response the most. Additionally, a crack detection method is proposed, identifying cracks based on the measured thermal response of a FOS cable and the air temperature, making it a very simple method to implement in the field by using only one measured DTS time series. This thesis acts as a solid stepping stone for future research in the field of crack detection via DTS.

1

Introduction

Climate change projections are showing more severe and frequent extreme drought events. In countries like The Netherlands, flood defenses, such as dikes, are affected by these drought events. The dike breach at Wilnis is an example of an incident not due to bad weather, but rather the result of a sunny summer. During the 2003 heat wave, the dike near Wilnis became dehydrated and the peat shrunk and cracked. The peat dike, normally saturated with water, became repellent to water and lost a great part of its weight. On 26 August 2003, at 02:00 the water pressure was too high for the dike to bear: the dike failed and flooded an entire residential area [6]. About 1500 citizens had to leave the area. Immediately after this incident, the Waterboards reinforced their peat dikes with clay, and protocols were drawn up for visual inspections.

More than 30% of the Dutch dike system consists of peat dikes [7]. Dikes having the biggest risk to fail are regional and most of them are part of a secondary flood defence lane located in 'het Groene Hart': a densely populated area with much low-lying polders. Unfortunately, these dikes belong to the most risky flood defense lanes in terms of failure. Drought events induce extra negative stresses in the soil, which result in the generation of cracks in the peat and clay covered dikes. These cracks can occur anywhere along kilometers in flood defenses, compromising their estimated safety standards. Drought affects the stability of peat dikes in four ways: water disappearing from pores having an unbeneficial effect on the dike's weight, occurrence of desiccation crack development, pressure of the underlying groundwater pushing the dike upwards which can cause the dike to float up (NL: opdrijving) and water-repellency of peat when drying out. The latter can be seen as the most dangerous, since the risk of dike breaches increases in this way if it rains: precipitation that is not absorbed by the soil can flow into the desiccation cracks causing erosion and eventually collapse.

Currently, it is not possible to identify the exact location of the cracks without having a human visual inspection along the dikes with a certain frequency prior to and during drought periods (Figure 1.1), mostly during spring and summer. These visual inspections vary significantly both per damage type and inspector, and the absence of a reference situation makes it difficult to estimate the severity of damages [8]. Furthermore, the waterboards handle different inspection thresholds on the precipitation deficit: some use $100mm$, others $200mm$, etc. [9], leading to incorrect maintenance measures. Additionally, visual maintenance inspections are expected to be less efficient in terms of capacity of inspected kilometers and highly prone to human errors.

The effect of desiccation cracks on dike failure and the processes involved when investigating desiccation crack development in peaty soils is already described in several studies. In a paper of Tang et al. [10] desiccation cracking characterization methods are summarized and reviews about the desiccation cracking behaviors of soils are given. Some articles make use of the power of the Finite Element Method (FEM) to gain knowledge about how cracks develop over time and which influences play important roles [11] [12]. Others make use of Distributed Temperature Sensing (DTS), Thermal Radiometric Camera (TRC), or webcam information, which can help investigate the phenomenon in the field. Schenato et al. [13] used Fiber Optic Sensor cable, used in DTS (FOS) to make predictions of the groundwater level. In another study of Lu et al. [14], visible images taken by drones were used to relate colors to groundwater level predictions. Cui and Chui [15] used temperature and water-level sensors to find the subsurface lateral heat fluxes between a reed bed and the adjacent water. And the

paper of Bense et al. [16] made use of DTS to find the thermal response of an uncracked soil.

This study couples FEM and DTS to develop a desiccation crack detection method and aims to better understand the influence of the most important environmental and thermal processes involved. For this, information found in studies of Juan Pablo Aguilar-López and Leonardo Duarte Campos is used [17], including a DTS study in summer 2021 at Flood Proof Holland, having a FOS cable on top of a cracked peat dike. The thermal information was calibrated and time series of the cable were retrieved. In the same period, webcam and thermal images of the cracked spot were taken. The results of the thermal camera were not corresponding with the results of the FOS cable. This thesis had been drawn up to investigate where this difference comes from, if a crack can be detected with DTS and to advice on improvements for further research. This will be done by means of a to-be-constructed finite element method (FEM) model, containing the experiment set up as it was in the Flood Proof Holland experiment. With this model, situations other than the measurement period (summer 2021) can be studied. It is expected that with the results found in this research, the processes influencing the thermal response of the system the most are mapped and a crack detection method using a FOS cable can be proposed. Figure 1.2 shows a scheme of the problem and expected solution. The research questions answered in this study have been drawn up to arrive at the final crack detection method and have not been formulated in the context of the Flood Proof Holland experiment. The first research question includes the construction of the FEM model and reads: **What is the best way to model the desiccation crack and the FOS cable in the peat dike at Flood Proof Holland with the use of FEM?** The second and third research questions include calibration and validation of the model: **How to calibrate and simulate the FOS experiment performed at Flood Proof Holland? What is the difference between the model and the experiment in terms of the thermal response of the cable?** After finishing the FEM model it is aimed to find the most important conditions influencing the thermal reponse of the cable so the fourth research question reads: **Which conditions have a significant influence on the thermal response of a FOS cable based on the FEM outcome?** This is done by performing multiple FEM studies and interpreting the thermal outcomes. Finally, a crack detection method is described by statistical time series analysis and the major research question can be answered: **What is the most optimal way to detect cracks using a FOS cable?**

The report starts with a methodology chapter explaining the research steps and the information needed to start the FEM model and is followed by the explanation of the FEM model and with it answering the first research question. Chapter 4 and 5 explain the calibration and validation of the model. In chapter 6 the outcomes of several FEM studies varying in model properties are given. Eventually, chapter 7 proposes a crack detection method using DTS data measured in the field. The results are interpreted and discussed in chapter 8. The report is closed by chapter 9 and 10 containing a general conclusion and recommendations for further research respectively.

Figure 1.1: Visual dike inspections during drought. [9]

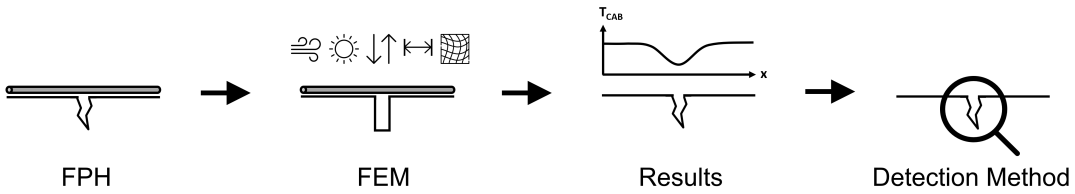

Figure 1.2: Problem scheme.

2

Methodology

It is expected that a relation between the modeled data and the field data will help to develop a prediction method for determining the temperature response of a crack and grass domain. This information may be useful for waterboards and other dike management organisations in two ways: to predict crack development in the future (maybe even to avoid this from happening) and to minimize visual inspections.

A FEM model is made to find the effect of the weather on a desiccation crack in a peat dike, consisting of four points in which data is obtained. CRK, CABCRK, GRS and CABGRS, all shown in Figure D.1. A crack domain, including a cable on top, is modeled to relate its thermal response to the temperature signal collected by an installed Fiber Optic Sensor cable (FOS) in an existent peat dike. In other words: the Fiber Optic Sensor cable, used in DTS (FOS) experiment is validated and compared with the outcomes of the FEM model constructed in this research. For calibration of the FEM model TRC data is used. More detailed information about the working principle of FEM models can be found in Appendix C.

Five research steps are followed which eventually result in a crack detection method using a fiber optic cable. Figure 2.1 gives a schematic overview of the research steps. The coming sections explain the methodology per research step.

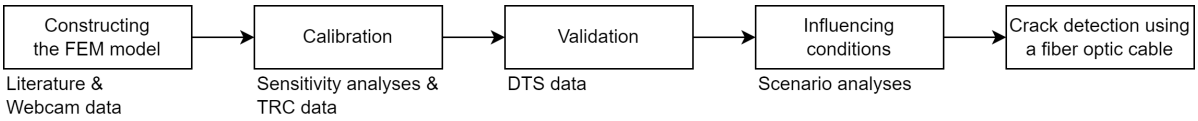

Figure 2.1: Research methodology in five steps: one step for each research question.

2.1. Constructing, calibrating and validating the FEM Model

Soil contains different kind of particles, also called grains. Because these grains are not perfectly square-shaped, there are voids. When these voids are filled with water, the soil is called fully saturated. The other situation is unsaturated, in which the voids are filled with air. Both conditions are shown in Figure 2.3a. In the same way, temperature flows from high to low and fluid flows from high head to low head. However, because of, among others, evaporation processes, a fully saturated condition is very unlikely to occur. Sometimes, these evaporation processes can be so intense that many of the water particles completely disappear from the soil, leaving the voids empty. The soil particles begin to separate and, due to an increase in tensile forces, cracks develop (Figure 2.2). Especially during drought periods, this is a common phenomenon. The interaction of particle size, soil structure, and plasticity influences the cracking behavior of soils after desiccation [18].

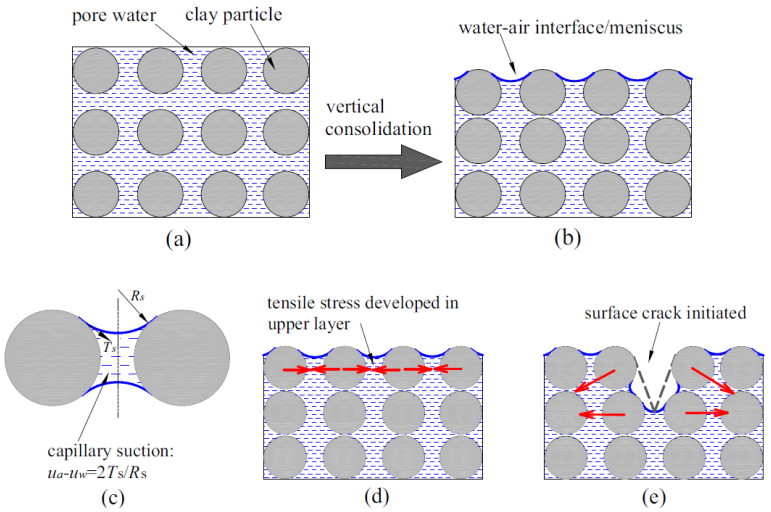

Figure 2.2: Crack initiation process: (a) initial fully saturated layer; (b) water-air interface meniscus developed between particles; (c) capillary suction between particles; (d) tensile stress developed in the upper layer; and (e) surface crack initiated. [10]

Soil desiccation is a multi-physics coupled process, involving the evolutions of water evaporation, volumetric shrinkage, and soil cracking [10]. For an initially saturated soil, the evaporation process generally takes place in three typical stages: (1) constant rate stage; (2) falling rate stage; and (3) residual rate stage [19]. To describe desiccation cracking, the soil cracking characteristic curve SCCC (R_{SC} versus water content, Figure 2.3b) can be consulted, in which R_{SC} is the surface crack ratio, which is the ratio of the surface crack area to the initial total surface area of a sample [20]. Considering the three stages of the evaporation process (Figure 2.3a), the shrinkage curve (Figure 2.3b) can be decomposed into three phases [10]. In the normal shrinkage phase, void ratio changes linearly with the water content, while the soil remains saturated. In this phase, the reduced soil volume is equal to the volume of water loss. The onset of cracking is observed within this phase and most cracks (80-90%) are formed (with a high water content or high levels of saturation, having low suction levels (Figure 2.3a.a and Figure 2.3a.b). When the water content decreases to the air entry point (= suction level at which air starts to penetrate into the soil), the soil shrinkage enters its residual shrinkage phase. In this phase, the volume shrinkage rate decreases. The reduced soil volume is smaller than the volume of water loss (Figure 2.3a.c). When the water content decreases further to the soil shrinkage limit, the soil structure reaches its dense state, with closer contact between the particles and negligible changes in volume and void ratio changes, also called the zero shirnkage phase (Figure 2.3a.d).

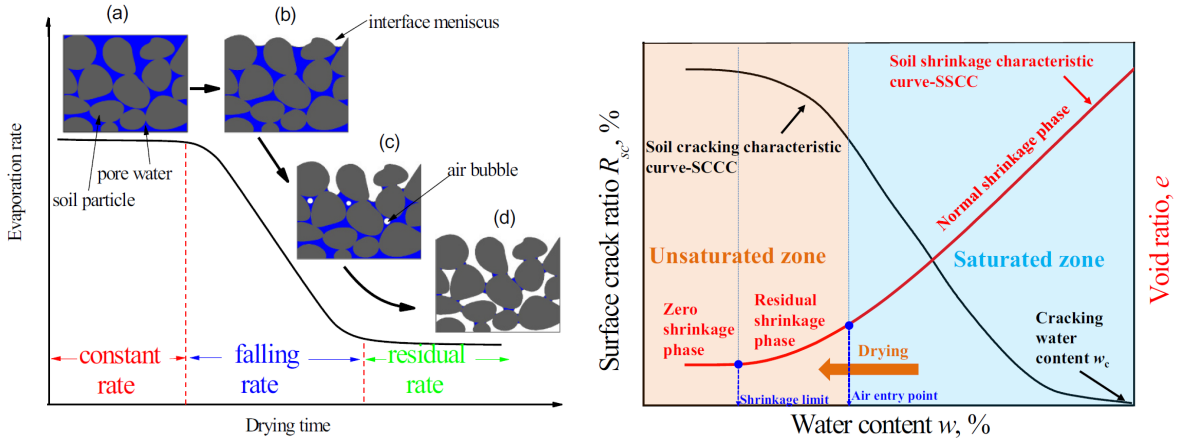

(a) (b)

Figure 2.3: The temporal evolution of evaporation rate for an initially saturated soil (a) and the evolution of surface crack ratio and void ratio with water content during drying (b). [10]

Heat flux $[Wm^{-2}]$ is the rate of thermal energy flow per unit surface area of heat transfer surface. It generalized into convection, radiation, and conduction. Figure 2.4 shows several examples. Convection is energy transfer due to a moving fluid, for example between wind and water (forced) or by differences in temperature (natural). Evaporation (form of convection) is heat transfer due to phase transition. When water is exposed to 100°C, it changes from fluid to gas, and due to this change in density, the heat flow moves upward. With radiation, no fluid flow but energy in the form of electromagnetic radiation is emitted by a heated surface in all directions and travels directly to its point of absorption at the speed of light. An intervening medium is not required to carry thermal radiation; there is no direct contact. Heat energy transferred by direct contact without any movement of the media is called conduction. An example of conduction is the heat flux between warm water and a cold subsoil.

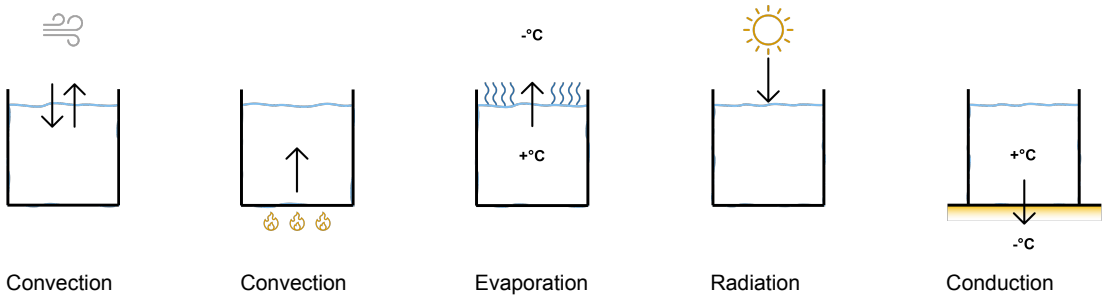

Figure 2.4: Examples of heat flow, indicated with arrows.

By finding the heat fluxes in the boundary layer of the model, the processes influencing the thermal response of the cable-crack system can be understood. Figure 2.5 gives an overview of the fluxes in the boundary layer. The latent heat flux is driven by the phase transition of liquid water from leaves to air. The sensible heat flux is related to changes in temperature of an object with no change in phase [21]. It is often referred to as the conductive heat flux from the Earth surface to the atmosphere, caused by the difference in temperature between the surface and the air (Equation 3.2). The FEM model is based on the heat balance equation (Equation 3.10). Each term in this equation is a heat flux. More information about the fluxes considered in this research can be found in section 3.8. The model is constructed using Figure 2.7. More information about how the model is constructed can be found in chapter 3. The calibration of the model with thermal images is given in chapter 4. The validation of the model with the DTS data can be found in chapter 5.

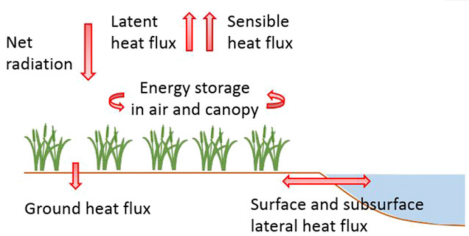

Figure 2.5: Fluxes in the boundary layer. [15]

2.2. Influencing Conditions

Having the FEM model validated, the model can be used to find the thermal responses and conditions influencing it the most for situations other than summer 2021. To find which characteristics influence the thermal response of the model, a scenario analysis is performed containing different model adjustments in each scenario, given in chapter 6. This section serves as the basis for the studies to be carried out.

2.2.1. Desiccation cracks in peat dikes

Peat dikes in The Netherlands were created during peat excavation in the course of the 16th century, serving as roads for the disposal of excavated peat. The top layer (approximately $1m$) was raised using

dried material from the peat farm [22]. During drought, water evaporates from the dike, which lowers the groundwater level and dries out the dike and, in areas with peaty subsoil, the underground as well. Volume shrinks in all directions, leading to shrinkage cracks and a decrease in dike volume, causing damage to slope instability or pipe failures. As a result, the total weight of the dike body decreases, becomes less strong, and the peat in the dike will have to absorb more shear strength to compensate for the decrease in strength. This leads to horizontal deformations, which, as a result of shrinkage, create a water pressure (in the sand layer just below the peat dike) that is much higher than the stationary water pressure in this sand. The dike can float, shear, and fail.

The groundwater level in peat dikes must be high to prevent biologically degradation above the groundwater level (oxidation). A rapid rise in the drainage level will not directly result in a rise in the phreatic surface in the peat dike and an increase in the weight of the occupant. The crown has been lowered as a result of shrinkage and will not swell again in a short time. Therefore, very heavy rain after a drought period can cause collapse and/or overflow, especially when the dike is not covered with clay and water can infiltrate in desiccation cracks.

On the other hand, if the groundwater level and therefore the phreatic line in the dike are in normal (higher) condition, heavy rain can still be a problem. The groundwater level rises even higher, creating a risk of shearing as well.

So, the stability of a peat dike is an important reason to maintain the level of the drainage basin and the polder water for as long as possible. In times of drought, water is sometimes supplied via a detour, in some cases resulting in higher water levels than the target, causing the dike to load more heavily. In extreme cases, it is possible to consider letting in brackish water, but the effect of brackish or salt water on the peat dike remains very unclear.

2.2.2. Crack position and geometry

The location of cracks over the dike depends on the distribution of suction-induced tensile stresses and the evolution of pore water pressure in the soil body, as well as microdefects and micropores [10]. However, it is assumed that desiccation cracks initiate at weak points on the soil surface. Most cracks initiate at the surface where the evaporation processes are higher. However, cracks can also initiate at lower soil levels [23]. Since this research focuses on surface crack detection this is not further investigated.

STOWA investigated the crack pattern and position in Prinsendijk, a peat dike located in 'het Groene Hart' of The Netherlands. The cracks in the dike crown mainly ran parallel to the elongation of the dike body, and the cracks on the slope had an orientation that varied from parallel to perpendicular to the extension of the dike body [24]. The cracks ranged in length from 0.15 to 2 m. The depth of the cracks was also variable, up to a maximum observed depth of about 0.15 m. Several studies give estimates of the depth of the cracks for desiccated soils [23] [25], with the main conclusion being that crack development is highly correlated with the water content and therefore occurs mainly in the unsaturated soil layer. Cracks form a pattern in desiccated soil bodies mainly composed of soil clods of triangle, quadrilateral and pentagon shapes, with cracks intersecting at 90°-150°[10].

2.3. Crack Detection Method

The study ends with a crack detection method advice when using DTS. The statistical time series analysis giving the easiest and best crack detection is proposed as crack detection method. Having the cracked spots mapped, the actual thermal response of the system can be found by correcting the DTS data. The cable measures the surface temperature but gets heated by radiation itself. This biases the measured thermal responses: the cable gives crack and grass temperatures higher than they are in reality. To find the thermal response of the cable, this extra heat by radiation has to be subtracted.

2.4. The Data

The measuring period took from **August 16, 2021 14:00 until September 6, 2021 8:00**. Including the FEM model, three information sources are present, shown in Figure 2.6. The KNMI, TRC and DTS data are shown in a time series format in Appendix B.

2.4.1. Flood Proof Holland (FPH) Dike

Flood Proof Holland is a test and showcase location for semi-full-scale temporary innovative modular and flexible flood defences [26] located in the south of Delft close by Delft University of Technology. The FPH dike where the experimental data was collected has a length of $20m$ and its width $4.5m$. On top of the dike a $200m$ long cable was laid in meandering pattern every $50cm$ (see Appendix A). The crack at FPH is monitored with a webcam, a Thermal Radiometric Camera (TRC) and a Fiber Optic Sensor (FOS). Regardless of the time steps the data were stored in (DTS 15 minutes for example), this study used 30 minute time steps for all data.

Webcam images Via webcam images the water content in the peat soil beneath the grass can be calculated using the grass greenness in the images.

Thermal images A Thermal Radiometric Camera (TRC) took thermal images of the crack during the measuring period. Two TRC time series were extracted from the data: the crack domain and the grass domain. The cable was distinguishable in the images, implying that TRC-CABCRK and TRC-CABGRS information can also be retrieved, but the pixel intensity was too small to obtain usable time series (about 3 pixels). The thermal images are uint16 images: having 2^{16} shades and 256×320 pixels per image. This pixel intensity can be transformed to temperature. The thermal images have been calibrated using the air temperature from the KNMI Rotterdam Airport measuring station (station KNMI 344).

Fiber Optic Sensor Besides a TRC, temperature data is measured via a black FOS cable, of $6mm$ in diameter, with a fiber inner core. The DTS data is a time series of every $25cm$ (spatial resolution) of cable of every 15 minutes. The process, called Distributed Temperature Sensing (DTS), is composed of the average of 10 points of $\pm 5.2cm$ (distance resolution), 5 left and 5 right (Figure A.4). When two light waves (injected from both ends) meet, the fiber shivers (literally) and an acoustic wave inside the fiber is created carrying information on the fiber's speed of sound – and, consequently, on its strain and temperature travelling towards the instrument [27]. The information is send (in matrix form) to a desktop PC. The DTS measurements were calibrated using the info recorded by a TD diver datalogger submerged in a cold bath with $15m$ of cable. With a lag correlation analysis it was found that there is a lag of 3 hours between DTS and the KNMI temperature. This lag was corrected for in the rest of the research. The plots in this report are already corrected for this lag.

2.4.2. KNMI data

The KNMI Rotterdam measuring station (344) is chosen for the ambient data. The data is stored hourly and can be found in Appendix B.

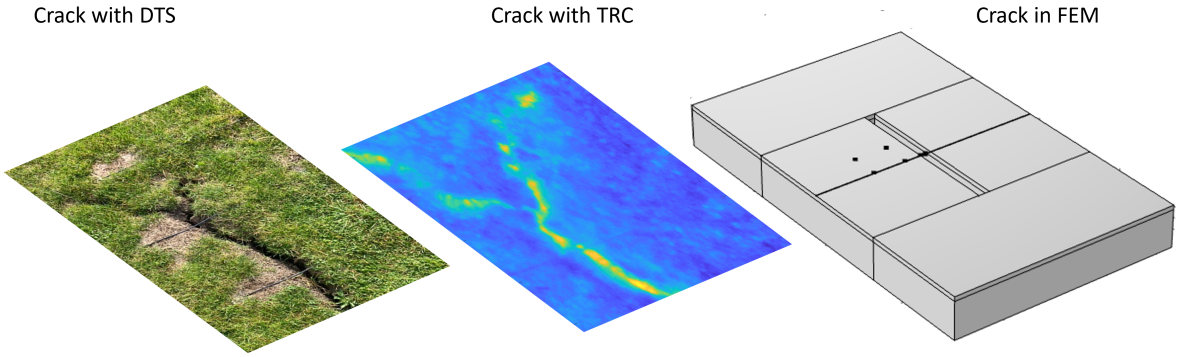

Figure 2.6: Three different information sources.

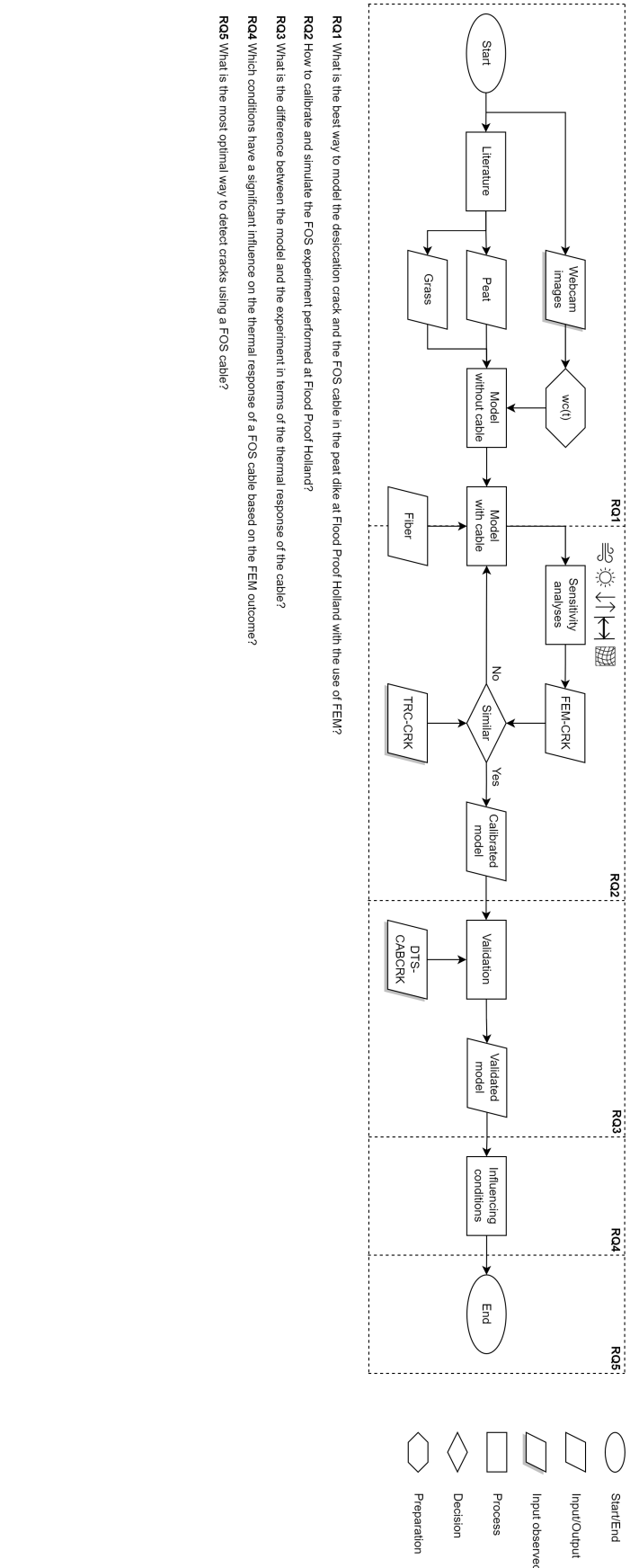

RQ1 What is the best way to model the desiccation crack and the FOS cable in the peat dike at Flood Proof Holland with the use of FEM?

RQ2 How to calibrate and simulate the FOS experiment performed at Flood Proof Holland?

RQ3 What is the difference between the model and the experiment in terms of the thermal response of the cable?

RQ4 Which conditions have a significant influence on the thermal response of a FOS cable based on the FEM outcome?

RQ5 What is the most optimal way to detect cracks using a FOS cable?

Figure 2.7: Flowchart of all model steps.

3

The Model

What is the best way to model the desiccation crack and the FOS cable in the peat dike at Flood Proof Holland with the use of FEM?

This chapter explains the constructed FEM model details. More information on the model dimensions and the FEM method used can be found in Appendix C and Appendix D. The chapter ends with a section explaining which thermal processes are included and which not.

3.1. Modeling a Crack

Heat flows from hot to cold areas. Assume that the x-axis is the direction of heat flow (one-directional) and the heat flows in a flat plate of thickness Δx and face area A with temperature difference ΔT (Figure 3.1). Heat flow, denoted by heat flux q $[W]$, is smaller for a thicker slab and larger for a greater temperature difference or larger face area. A relationship is found.

$$q \propto A\frac{\Delta T}{\Delta x} \tag{3.1}$$

Rewriting this relationship into an equation requires the introduction of thermal conductivity $k[Wm^{-1}K^{-1}]$. Thermal conductivity is a measure of a material's ability to conduct heat. Good electricity conductors are also good thermal conductors. Metals, for example, have higher thermal conductivity compared to insulation materials. The equation known as Fourier's law is shown in Equation 3.2. This equation relates the heat flux and temperature with thermal conductivity.

$$q[Wm^{-2}] = -k[Wm^{-1}K^{-1}] \cdot \frac{dT(x)[K]}{dx[m]} = -k \cdot \Delta T \tag{3.2}$$

Another important term in heat transport is heat capacity. It is defined as the object's ability to store energy in the form of heat. Heat capacity is denoted with $C[Jkg^{-1}K^{-1}]$.

$$Q[J] = C[Jkg^{-1}K^{-1}] \cdot m[kg] \cdot \Delta T[K] \tag{3.3}$$

The relationship between thermal conductivity and heat capacity is called thermal diffusivity (α), which is the rate of heat transfer from hot to cold. In other words: it is a measure of thermal inertia. The higher the thermal diffusivity, the faster the heating/cooling of the material. The material acts as a conductor. The lower the thermal diffusivity, the slower the heating/cooling of the material (heat storage). The material acts as a insulator.

$$\alpha[m^2s^{-1}] = \frac{k[Wm^{-1}K^{-1}]}{\rho[kgm^{-3}] \cdot C[Jkg^{-1}K^{-1}]} = \frac{\text{heat conducted}}{\text{heat stored}} \tag{3.4}$$

$$\frac{1}{\text{thermal diffusivity } (\alpha)} \sim \frac{1}{A_{\text{ptp}}} \tag{3.5}$$

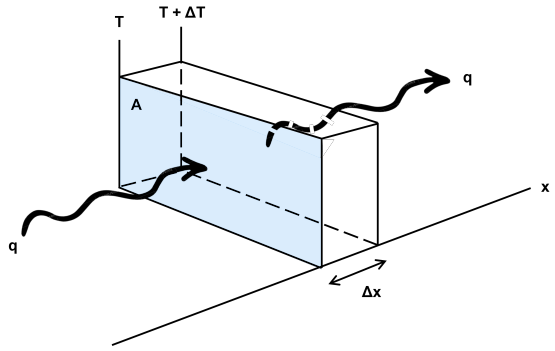

Figure 3.1: One-directional heat flow.

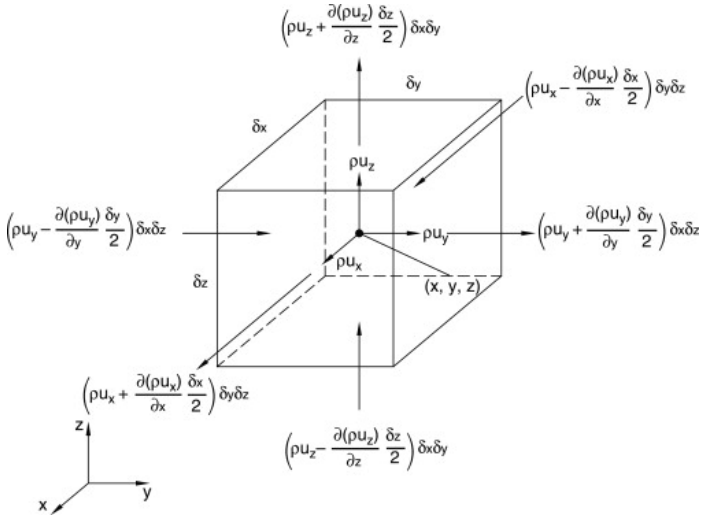

Figure 3.2: Mass flux through an infinitesimal element control volume. [28]

Assume a square element with volume V and surfaces A that is subject to an incoming and outgoing mass in the x-direction only m_x (Figure 3.1). Inflow or outflow mass is the result of the speed (u) with which the flow enters or leaves the volume element. The mass flux becomes as follows:

$$\dot{m}_x = \frac{dm_x}{\Delta A \cdot dt} = \frac{dV_x \cdot \rho_x}{\Delta A \cdot dt} = \frac{(\Delta A \cdot u_x \cdot dt) \cdot \rho_x}{\Delta A \cdot dt} = \rho_x \cdot u_x \tag{3.6}$$

The continuity equation is an expression representing the idea that the mass is conserved in a flow. Per unit volume, the sum of all masses that flow in and out per unit time must be equal to the change in mass due to the change in density per unit time [28].

$$\frac{\partial}{\partial t} m_{element} = \dot{m}_{in} - \dot{m}_{out} \tag{3.7}$$

Substituting Equation 3.6 into Equation 3.7 for all directions (Figure 3.2) gives the continuity equation shown in Equation 3.8.

$$\begin{aligned} \frac{\partial \rho}{\partial t} &= -\left(\frac{\partial \rho}{\partial x} u_x + \frac{\partial \rho}{\partial y} u_y + \frac{\partial \rho}{\partial z} u_z\right) \\ \frac{\partial \rho}{\partial t} &+ \nabla \cdot (\rho \underline{u}) = 0 \end{aligned} \tag{3.8}$$

This continuity equation forms the basis for the energy balance shown in Equation 3.9, describing the amount of heat transferred per unit of time (heat transfer rate) in which the first term in the equation accounts for accumulation (change of mass in the system or variations of internal energy), the second term convection of internal energy (difference in inflow and outflow), the third term thermal conduction, the fourth term radiation, and terms on the right-hand side are heat sources and sinks.

$$\rho\left(\frac{\partial E}{\partial t} + u \cdot \nabla E\right) + \nabla \cdot (q_{cd} + q_r) = Q_0 \tag{3.9}$$

Equation Equation 3.10 shows the heat balance equation, derived from the energy balance shown in Equation 3.9. This heat balance forms the basis of the FEM model. The FEM model consists of a Heat Transfer interface, accounting for all temperature fluxes in the system. The influence of the Sun and its radiation is included via the term Q_r, and is found using a Radiation interface in the FEM model (more information in section 3.7). The required model inputs are found through a literature study and by the data (section 2.4).

$$\rho C\left(\frac{\partial T}{\partial t} + \cancel{+u \cdot \nabla T}\right)^{0} + Q_{cd} + Q_r = Q_0 \tag{3.10}$$

$Q[Wm^{-3}] = \nabla q = \frac{\partial q_x}{\partial x} + \frac{\partial q_y}{\partial y} + \frac{\partial q_z}{\partial z}$
$\rho C \frac{\partial T}{\partial t}$ = internal energy
$\rho C u \cdot \nabla T$ = internal convective heat flux = 0 (no fluid domains modeled)
$q_{cd}[Wm^{-2}]$ = conductive heat flux = $-k\nabla T$
$q_r[Wm^{-2}]$ = radiation heat flux = $\epsilon(G - \sigma \cdot T^4)$
$q_0[Wm^{-2}]$ = inward convective heat flux = $h(T_{KNMI} - T)$

A scheme of the constructed FEM model is shown in Figure 3.3. The model consists of three model domains: grass, peat and cable. Equation 3.10 is solved for T for every element in the FEM model.

In order to optimally compare the modeled crack with the actual crack, the dimensions of the FEM crack should preferably be the same as the dimensions of the actual crack in Flood Proof Holland. The latter are shown in Appendix A. The cable diameter amounts $6mm$, the thickness of the grass layer is assumed to be $4cm$, and the subsoil is set to twice the depth of the crack, consequentially $34cm$. The initial values are used as starting temperatures at $t = 0$ for a study. Here, the mean KNMI temperature during the measurement period is taken. The model inputs are used throughout the study as inputs for the equations. The influence of the air (convection) and radiation are included as boundary conditions. More information on convection and radiation in Figure 3.4a can be found in section 3.6 and section 3.7. The third boundary condition (Figure 3.4b) is a linear temperature distribution between the surface temperature and the temperature at the bottom of the peat layer. This bottom temperature (Figure 3.4c) is set to a constant value over time of $15°C$. A constant temperature is needed to keep the system understandable and has no noticeable influence on the points used for the outcomes. A temperature of $15°C$ is chosen because it corresponds with the average KNMI temperature during the measurement period.

3.2. Modeling a FOS cable

The actual FOS cable in the field at Flood Proof Holland consists of several layers of material, with the inner core being fiber. Due to these layers, an extremely fine mesh of millions of elements is needed, resulting in computational problems. Fortunately, it is found that the temperature differences between these layers are negligible if the external temperature varies just as slowly in time for the layers to respond (Figure 3.5). The air temperature varies by a few degrees per hour, which turned out to be slow enough for the layers to respond sufficiently: so the inner layers do not have to be modeled. The material properties of the cable were calibrated in a previous study, based on the catalog of the cable producer, and therefore, they no longer have to be calibrated. The cable is assumed to be 50% embedded in the soil.

3.2.1. Final model

The influence of radiation, therefore the cable's embeddedness, is an important aspect to consider. Throughout this investigation, a cable embeddedness of 50% and emissivity values calibrated by parametric sweeps are used. Eventually, after the research has been completed, an adjusted final model is described using realistic embeddedness and emissivity values. This model is referred to as the 'final model' and should be used in further research. The variations between these models are shown in Table 3.1.

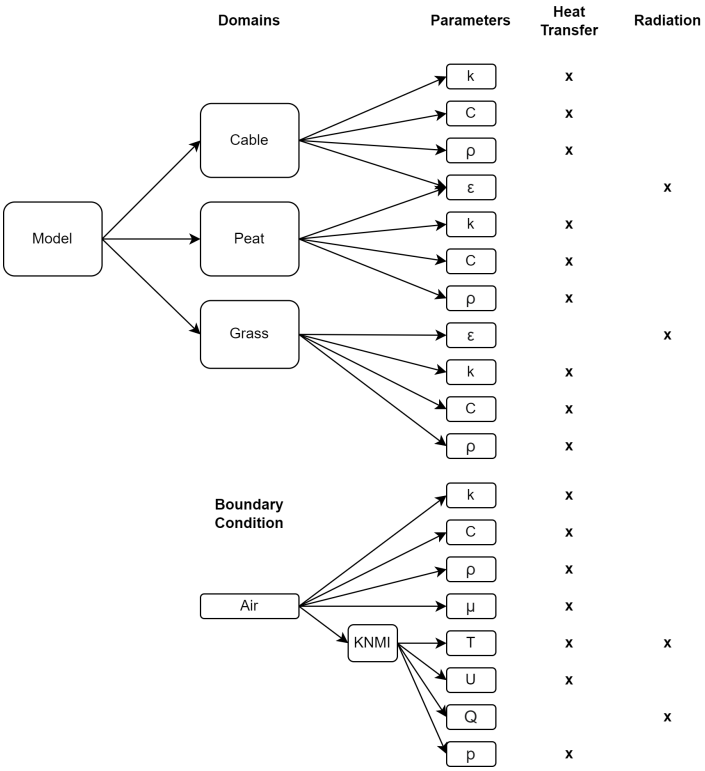

Figure 3.3: FEM model construction, in which is shown which parameter is needed for either the Heat Transfer or Radiation interface. Air is not included as a domain but its influence is implemented as a boundary condition for both Heat Transfer and Radiation, as described in section 3.6 and section 3.7

.

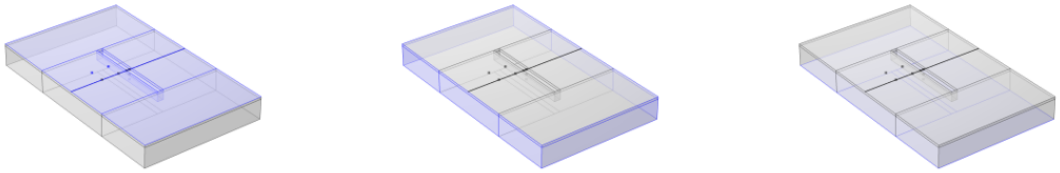

(a) Convection & radiation. (b) Linear temperature distribution. (c) Constant temperature $(15°C)$

Figure 3.4: Boundary conditions applied in the FEM-model.

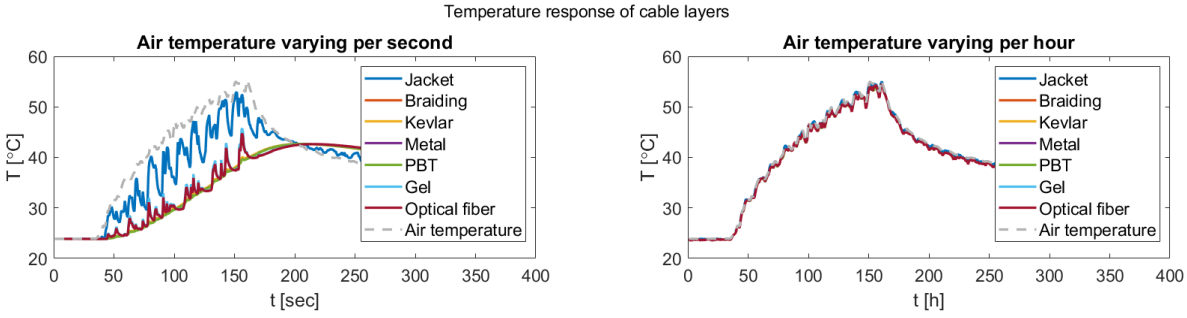

Figure 3.5: Thermal response of the cable's inner layers to a varying temperature in seconds (left) and hours (right).

3.3. Modeling a Grass Canopy

The thermal conductivity of grass depends on the water content between the grass leaves. A simplified model is used (Figure 3.6) in which the moisture transport is directed only in the vertical direction. Subscripted abbreviations (single letter and combined) are used to indicate air a, grass g, and water w. The water content is indicated by wc and the thermal conductivity by k. The radius of a grass leave is denoted by a, the distance between two grass leave cores is denoted by b and the height of the grass canopy is denoted by d.

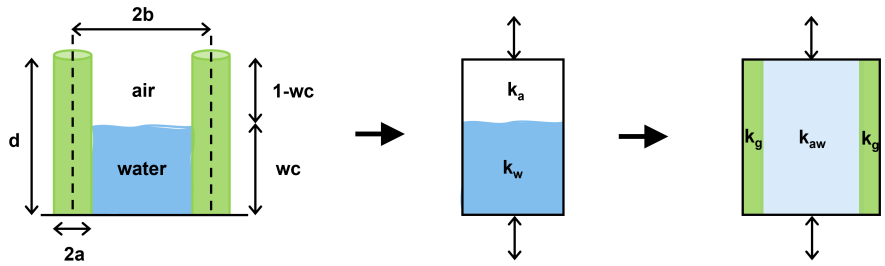

Figure 3.6: Model (composed of combination of series and parallel) for determining the thermal conductivity of grass.

The thermal conductivity of water and air together is calculated using the formula for series.

$$k_{aw}(wc)[Wm^{-1}K^{-1}] = \frac{k_a \cdot (1 - wc) + k_w \cdot wc}{1} \tag{3.11}$$

The grass is included using a parallel formula.

$$k_{gawg}(wc)[Wm^{-1}K^{-1}] = \frac{a + 2b - 2a + a}{\frac{a}{k_g} + \frac{2b-2a}{k_{aw}(wc)} + \frac{a}{k_g}} \tag{3.12}$$

The assumed values can be found in the List of Symbols on page xiii. This thermal conductivity is also according to Lu et al. [29], stating that the higher the thermal conductivity (k), the higher the water content in the material.

The density of the grass canopy, depending on its water content, is estimated in the same way as the thermal conductivity.

$$\rho_{grass}(wc)[kg \cdot m^{-3}] = \frac{2\rho_g(a \cdot d) + d\rho_w wc(2b - 2a) + \rho_a(1 - wc)(2b - 2a)}{a \cdot d \cdot 2 + d \cdot wc(2b - 2a) + d(1 - wc)(2b - 2a)} \tag{3.13}$$

The heat capacity of a grass canopy that includes water and leaves, depending on its water content, is found using Campbell and Norman [30].

$$C(wc)[Jkg^{-1}K^{-1}] = (1 - \theta_g)(wc \cdot C_w + (1 - wc) \cdot C_a) + \theta_g C_g \tag{3.14}$$

The water content (wc) is the same as used in Equation 3.11. From the relationship between the grass leaves and the water / air column shown in Figure 3.6 it is found that the ratio of grass leaves and leave distance $\theta_g = \frac{2a}{2b} = \frac{a}{b}$.

3.4. Modeling a Peat Column

Peaty soils consists of solid peat, water and air. The density of a peaty subsoil is, among others, dependent on its water content, which varies over time, and its porosity n, as shown in Figure 3.7. Since the FEM model is heat only, water transport is not important and the water content in the peat must be included.

(a) Peat subsoil in Schotland [31]

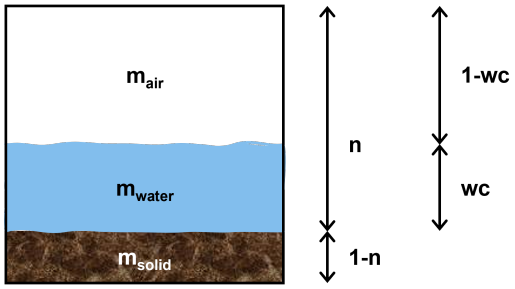

(b) Relationship between water content (wc) and porosity (n).

Figure 3.7: Peat composition.

Cylindrical samples taken at FPH, with diameter D and length L , provide the correct values for Equation 3.21, as also given in the List of Symbols on page xiii.

$$\begin{aligned} \rho_{p,bulk}[kgm^{-3}] &= 1010 \\ \rho_{p,dry}[kgm^{-3}] &= 130 \\ D[mm] &= 67 \\ L[mm] &= 26 \end{aligned}$$

$$mc[-] = \frac{\rho_{bulk}}{\rho_{dry}} - 1 = \frac{1010}{130} - 1 = 6.77 \tag{3.15}$$

$$V_{tot}[m^3] = \pi \cdot (0.5 \cdot D[mm])^2 \cdot L[mm] \cdot 10^{-9} = \pi \cdot (0.5 \cdot 67)^2 \cdot 26 \cdot 10^{-9} = 9.2 \times 10^{-5} \tag{3.16}$$

$$m_{solid}[kg] = \rho_{dry} \cdot V_{tot} = 130 \cdot 9.2 \times 10^{-5} = 1.2 \times 10^{-2} \tag{3.17}$$

$$m_w[kg] = mc \cdot m_{solid} = 6.77 \cdot 1.2 \times 10^{-2} = 8.1 \times 10^{-2} \tag{3.18}$$

The water content in the cylindrical samples at FPH can be calculated with Equation 3.19.

$$wc[-] = \frac{m_w}{m_{soil}} = \frac{m_w}{m_w \cdot \left(1 + \frac{1}{mc}\right)} = \frac{8.1 \times 10^{-2}}{8.1 \times 10^{-2} \cdot \left(1 + \frac{1}{6.77}\right)} = 0.87 \tag{3.19}$$

With the porosity of $n = 0.9$ [4], $\rho_{bulk}(wc)$ can be found, by calculating $m_w(wc)$ through Equation 3.20 and calculating $\rho_{bulk}(wc)$ after using Equation 3.21.

$$m_w(wc)[kg] = \rho_w \cdot V_w = \rho_w \cdot n \cdot wc(t) \cdot V_{tot} \tag{3.20}$$

The total density dependent on the water content that has to be implemented in the FEM model becomes:

$$\rho(wc)[kgm^{-3}] = \frac{m_w + m_{solid}}{V_{tot}} = \frac{1000 \cdot 0.9 \cdot wc(t) \cdot 9.2 \times 10^{-5} + 1.2 \times 10^{-2}}{9.2 \times 10^{-5}} = \frac{0.0828wc(t) + 1.2 \times 10^{-2}}{9.2 \times 10^{-5}} \tag{3.21}$$

The thermal conductivity and heat capacity of peat are found using graphs for different types of peat of Zhao and Si [32]. Randstad peat dikes, like the peat dike located at FPH, have a peat ratio of approximately 20 to 40% [33] [34], which means that the PS23 and PS14 lines in Zhao and Si should be followed [32]. The volumetric heat capacity $[MJm^{-3}K^{-1}]$ is related to the specific heat capacity $[Jkg^{-1}K^{-1}]$ by density (Equation 3.22). To be consistent in this transformation from volumetric to specific, the peat density of Zhao and Si [32] is taken only for the transformation ($\rho = 1400kgm^{-3}$) and not as a model input. Equation 3.21 is used as model input.

$$C[Jkg^{-1}K^{-1}] = \frac{C_p[Jm^{-3}K^{-1}]}{\rho[kgm^{-3}]} \tag{3.22}$$

Finally, both material properties can be approximated with Equation 3.23 and Equation 3.24. The graphs are shown in Appendix D.

$$C(wc)[Jkg^{-1}K^{-1}] = 3295.9 \cdot wc + 658.16 \tag{3.23}$$

$$k(wc)[Wm^{-1}K^{-1}] = 3 \cdot wc + 0.2 \tag{3.24}$$

3.5. Modeling Water Content

As given in subsection 2.2.2, the water content in a soil is highly related to crack development, with cracks mostly in unsaturated soil layers. As explained in earlier sections in this chapter, the FEM model material properties are all water content dependent (see graphs in Figure D.2). A constant water content can be used, but a time series of a water content ($wc(t)$) is preferred. When substituting this time series in the equations explained in section 3.3 and section 3.4, the grass and peat material properties vary over time, aiming to more actual FEM model outcomes.

According to Lu et al. (2020) [14] the water content of the upper 0-10 cm subsoil ($wc(t)$) is related to the brightness (B) of a visible image. For a water content greater than 5% this relationship is given by Equation 3.25, in which the brightness of an image can be found by the grayscale of the image. This brightness is found using webcam images taken of the FPH dike. $wc(t)$ can thus be calculated by webcam images. Images at night (between 19:00 and 7:00) were not considered, since they were not usable due to the absence of sunlight. Instead, the data at night was linearly interpolated between the water content values at 19:00 and 7:00.

Figure 3.8 shows the water content outcome based on the approach described above, used as model input for the FEM model. As an indication the air temperature is plotted too, being a driver of the water content time series.

$$wc(t)[\%] = 70.52 - 0.47B(t) \tag{3.25}$$

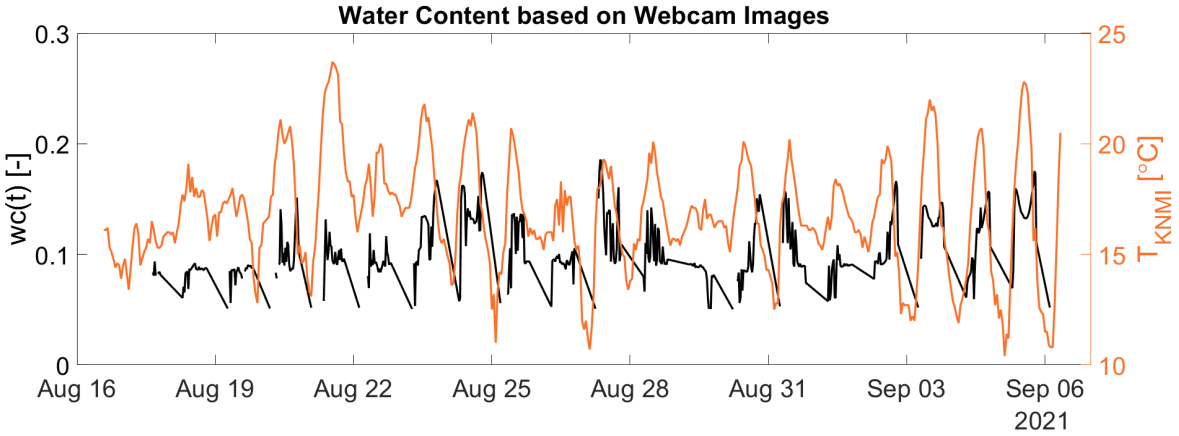

Figure 3.8: Left axis: water content based on the webcam images (black), water content values range from 0 to 1 but axis is limited to 0.3. Right axis: air temperature measured by KNMI (orange).

3.6. Modeling Wind, Temperature and Pressure

The dike surface is exposed to the wind, temperature, and pressure of the environment. Addressing these influences, which can be termed forced convection, can be done in two ways. The first way is to model the air domain (fluid) on top of the crack and soil domains. This approach gives reliable results, but also a huge computation time, since it solves for the fluid flow in the air domain. The second way is to model the heat transfer by using heat transfer coefficients in a heat flux boundary condition, which has the advantage that the air domain does not have to be modeled, resulting in a faster computation time. A disadvantage is that a simple geometry is required when using heat transfer coefficients. The sensitivity analysis for both method is shown in section 4.1. Due to the negligible difference in results and lower computation time of the second method, the choice is made to use an external forced convection heat flux on the surface boundaries. This heat flux is added on the right-hand side of Equation 3.10.

$$q_0[Wm^{-2}] = h \cdot (T_{KNMI}(t) - T(t)) \tag{3.26}$$

$h[Wm^{-2}K^{-1}]$ = averaged heat transfer coefficient according to the Nusselt number correlation
$T[K]$ = internal temperature calculated by COMSOL

The average heat transfer coefficient is calculated according to the correlations developed by Churchill [35] and Rose [36].

$$h[Wm^{-2}K^{-1}] = \frac{2 \cdot Nu_l + Nu_t \cdot k_{air}}{L} \tag{3.27}$$

$$Nu_l[-] = \frac{0.3387 Re^{1/3} Pr^{1/3}}{\left(1 + \left(\frac{0.0468}{Pr}\right)^{2/3}\right)^{1/4}} \tag{3.28}$$

$$Nu_t[-] = \left(0.037 Re^{4/5} - 871\right) Pr^{1/3} \tag{3.29}$$

$$Re[-] = \frac{\rho_{air} \cdot U_{KNMI}(t) \cdot L}{\mu_{air}}$$

$$Pr[-] = \frac{\mu_{air} \cdot C_{air}}{k_{air}}$$

Re = Reynolds number: laminar (l) if $Re \leq 5 \times 10^5$ and turbulent (t) if $Re > 5 \times 10^5$
Nu = Nusselt number
Pr = Prandtl number
L = representative length, in this case the dike's crest width being $1m$
$\rho_{air}, \mu_{air}, C_{air}, k_{air}$ = dependent on ambient pressure p_{KNMI} and found in the COMSOL air material

3.7. Modeling Radiation

The radiative heat source (Q_r in Equation 3.10) is added to the boundaries exposed to radiation.

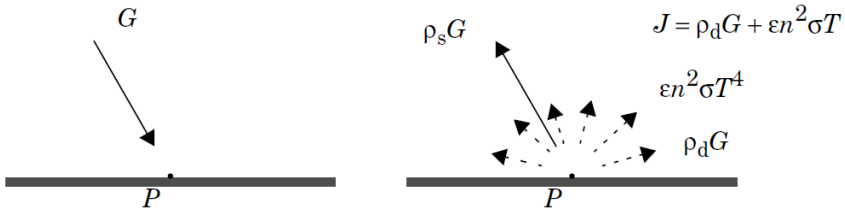

Figure 3.9: Incoming irradiation (direct and diffusive) G, outgoing radiosity J and scattered irradiation by the body $\rho_s G$. [37]

The net inward radiative heat flux into an opaque body is given by the difference between three types of radiative fluxes.

$$q_r(t) = G(t) - \rho_s G(t) - J(t) \tag{3.30}$$

The total incoming radiative flux is called irradiation (G). A part of this is being scattered by the surface ($\rho_s G$) and the total outgoing radiative flux is called radiosity (J). Assuming that the surface is part of an ideal gray body (absorptivity equal to emissivity) and Equation 3.30 can be simplified to Equation 3.31.

$$q_r(t)[Wm^{-2}] = \epsilon \left(G(t) - e_b(T(t))\right) \tag{3.31}$$

$\epsilon[-]$ = surface emissivity
$e_b(T(t))[Wm^{-2}]$ = blackbody hemispherical total emissive power = $n^2 \sigma T(t)^4$
$n[-]$ = refractive index air = 1
$\sigma[Wm^{-2}K^{-4}]$ = Stefan-Boltzmann constant
$T(t)[K]$ = calculated FEM temperature

$$G(t)[Wm^{-2}] = G_m(t) + G_{amb}(t) + G_{ext}(t) \tag{3.32}$$

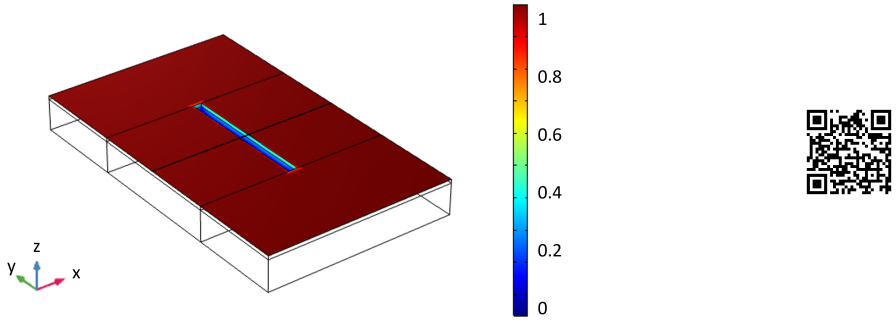

Figure 3.10: View factors. Left: Ambient view factor, constant in time. Right: External source view factor.

$G_m(t)$ = mutual irradiation (coming from other boundaries or radiation sources in the model)
= 0
$G_{amb}(t)$ = ambient irradiation = $F_{amb}\epsilon_{amb}\sigma T_{KNMI}(t)^4$
$F_{amb}[-]$ = ambient view factor (Figure 3.10a)
= fraction of the field of view that is not covered by other boundaries, constant in time
= $0 \leq F_{amb} \leq 1$.
= 1 (sun = blackbody)
$G_{ext}(t)$ = external radiation sources (sun)

$$\begin{aligned} G_{ext}(t)[Wm^{-2}] &= q_{0su} &+ I_{diff} \\ &= F_u(t) \cdot Q_{KNMI}(t) \cdot FEP &+ 0 \end{aligned}$$

$I_{diff}[Wm^{-2}]$ = diffusive irradiance (already included in Q_{KNMI})
$FEP[-]$ = fractional emissive power
= 1 (surface emissivity is defined the same for short and long wavelengths)
$Q_{KNMI}[Wm^{-2}]$ = surface radiation measured by KNMI
$F_u(t)[-]$ = view factor dependent on the position of the sun, varying in time (Figure 3.10b)
= $0 \leq F_u \leq 1$.

External radiation can be modeled as an external rotating radiation source (being the sun) with irradiance $Q_{KNMI}(t)$. Cartesian coordinates are used, with the north, west, and up directions being the x, y, and z directions, respectively. A drawback of this method is that the Sun's rotation is twice included here: in the dataset of $Q_{KNMI}(t)$ and once again when including the rotation of the Sun in the view factor. However, view factors have to be included to account for shadowing effects at, for example, the bottom of the cable on top of the crack, and a more detailed way of modeling is not present since applying $Q_{KNMI}(t)$ to all surfaces exposed to the Sun will not include shadowing effects.

$Q_{KNMI}(t)$ is the sum of direct and diffusive radiation (both incoming fluxes) [38]. Sunlight falling directly on the Earth's surface is called direct radiation. Unlike diffusive radiation, sunlight falls on the Earth's surface without any hindrance. On the other hand, the term "diffuse" implies that the light arrives irregularly and with no uniform direction. This is the case when sunlight penetrates through clouds or changes direction and/or intensity due to other particles in the air, for example, when there is water vapor, dust, or pollutants in the air. $Q_{KNMI}(t)$ therefore does not consist of reflected radiation.

The grass is modeled as a solid domain, which is not. It is a green surface that contains grass leaves where water and air are present in between. To include the effect of air and water between grass leaves (air does not absorb radiation from the sun, grass leaves and water do), the average water content is used during the measurement period, being $9.24\% \approx 0.1$ (Figure 3.8). The ratios shown in Figure 3.6, the grass domain includes 5% of grass leaves, 10% of water, and 85% of air. Grass leaves have a leave emissivity ϵ of about 0.97 [39] and water approximately 0.9 [40]. The emissivity of the grass surface becomes $0.05 \cdot 0.97 = 0.05$ for the leaves and $0.1 \cdot 0.9 = 0.1$ for the water, thus between 0.05 and 0.1. In this study a value of 0.05 is used.

Not much literature can be found on the emissivity of peat soils. In Figure 3.7 it is shown that the peat domain is composed of solid, water, and air. The emissivity of the peat domain is influenced by

porosity n and water content wc. Figure 3.8 shows that the peat was dried out and contained little water and a lot of air. In researches of Thompson et al. [41] and Gerber et al. [42] emissivity values of about 0.8-0.9 are found for peat and dried leaves. Here a value of 0.95 is used.

In the literature, the emissivity of a black rubber cable is found to be 0.9 [40]. In the model, the cable is for 50% embedded in the soil, and an emissivity of 0.4 gives consistent results with the DTS data. Using a realistic emissivity value of about 0.9, the cable has to be embedded for 95% in the soil to respond the same as the DTS data. These results show that the cable is heavily influenced by radiation. More information about this influence is given in section 4.1.

Table 3.1: Surface emissivity-values for the model used throughout this research and the final model as described in subsection 3.2.1.

Material	**Emissivity (ϵ) for 50% embeddedness**	**Emissivity (ϵ) for 95% embeddedness**
Peat	0.95	0.95
Grass	0.05	0.05
Cable	0.4	0.95

3.8. Fluxes in the Model

Figure 2.5 shows the different energy fluxes in the boundary layer. Some of the fluxes shown in this figure are not taken into account in the FEM model. Since there is no water present in the model, the horizontal lateral energy exchange between water and soil is not taken into account. Furthermore, phase transitions are not included in the model. Water is a constant element that is included as an input in the material properties, so the vertical latent heat flux is not taken into account.

The radiation flux Q_r is positively throughout the measuring period (Figure 3.12), bringing energy into the system. The sensible heat flux Q_0 for the crack is in sign the same as Q_r (Figure 3.12). It brings energy into the crack during the day and releases it during the night. During the day, the air temperature heats the crack, giving it energy. During the night, the crack is warmer than the environment (also shown in Figure 4.4a) and gives back the energy stored during the day. For grass, this convective heat flux Q_0 is almost completely negative even for the whole measuring period. The FEM grass temperature is always warmer (during day and night) than the air temperature, as shown in Figure 4.4a. Since the radiation is the same for the whole system, apparently grass is more sensitive to radiation and warms up faster compared to peat. Its thermal conductivity k is in fact much smaller than that of peat, indicating that grass conducts heat faster than peat (Figure D.2). The conduction flux Q_{cd} is generally positive during the night (energy is stored) and negative during the day (energy is released) (Figure 3.12). This has to do with the definition of Q_{cd}, which is Fourier's law (Equation 3.2), containing a minus sign.

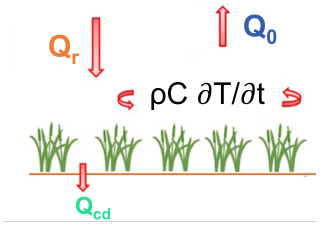

Figure 3.11: Fluxes considered in the FEM model, indicated with terms of Equation 3.10.

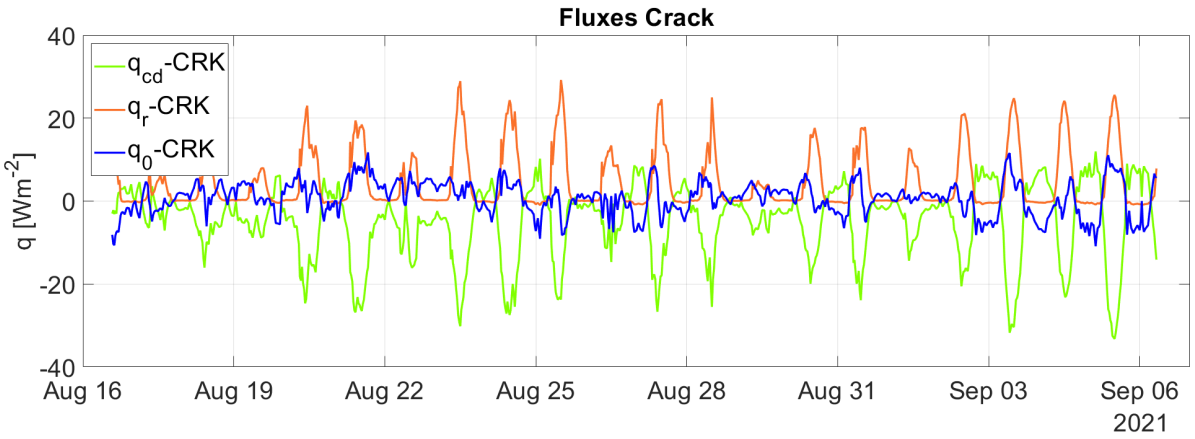

(a) Crack point (bottom).

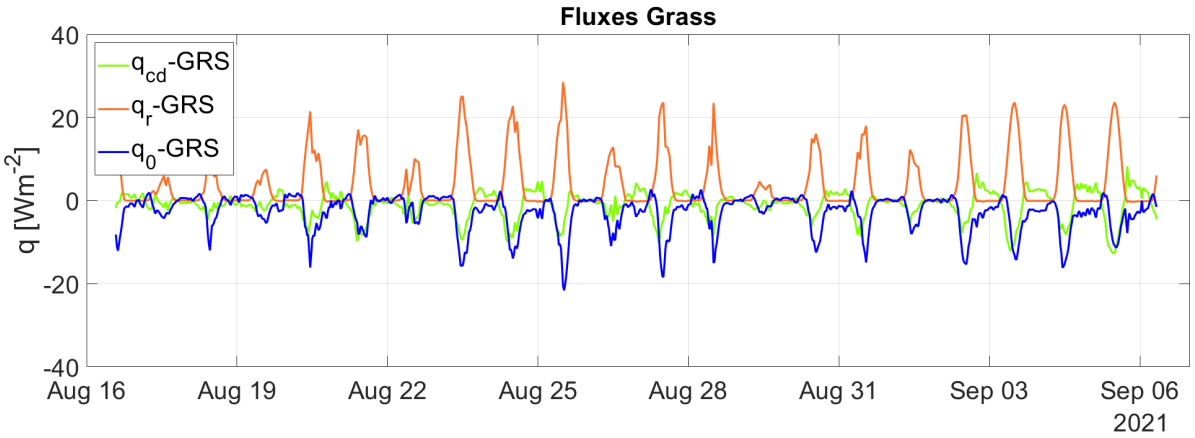

(b) Grass point.

Figure 3.12: Fluxes in the model. Positive values indicate inward fluxes. Negative fluxes extract energy from the model.

4

Calibration

How to simulate and calibrate the FOS experiment carried out at Flood Proof Holland?

After finishing the construction of the FEM model it must be calibrated. Figure 4.1 shows the steps taken in this chapter. The calibration of the model starts with a sensitivity analysis to check its behavior while changing model properties. After this, the Thermal Radiometric Camera (TRC) data are used to calibrate the bottom of the modeled crack and the grass.

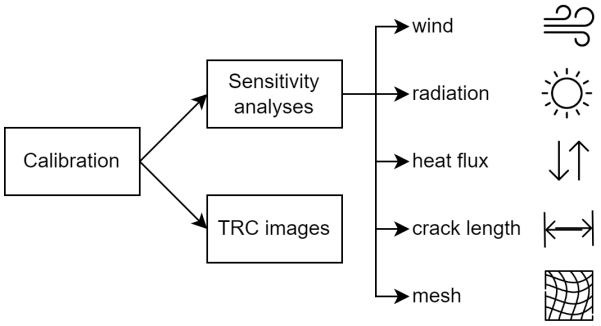

Figure 4.1: The two calibration steps: first performing sensitivity analyses and second calibrating with TRC images.

4.1. Sensitivity analysis of wind and radiation

As given in section 3.6 modeling a wind domain is computationally more intensive than modeling these ambient effects in a boundary condition. To find whether the ambient properties can be modeled with a boundary condition, three studies are described by the three lines in Figure 4.2. The first study includes only soil domains in which the influence of the ambient properties is modeled via the heat flux boundary condition and radiation is included. The second study includes air domains for the crack and first 10 meter of air above the ground. The wind travels in the x direction and the radiation is included. The last study is the same as the second study, except by the fact that the Radiation interface is turned off, so the influence of radiation is none. As can be concluded, modeling of air domains is not necessary. The less computationally intensive heat flux boundary condition can be used, in which the geometry contains only cable, grass, and peat domains, and no air domains.

4.2. Sensitivity analysis of cable embeddedness

To find the emissivity value of the modeled half-embedded cable, a parametric study is performed. The emissivity of the cable above the crack is not influenced by this embedding. An emissivity of 0.4 turned out to be already enough for the FEM-CABGRS point to correspond to the DTS data, which implies that 60% of the radiation from the Sun is not absorbed by the cable and in literature emissivity values for cables like these are 0.95 (section 3.7).

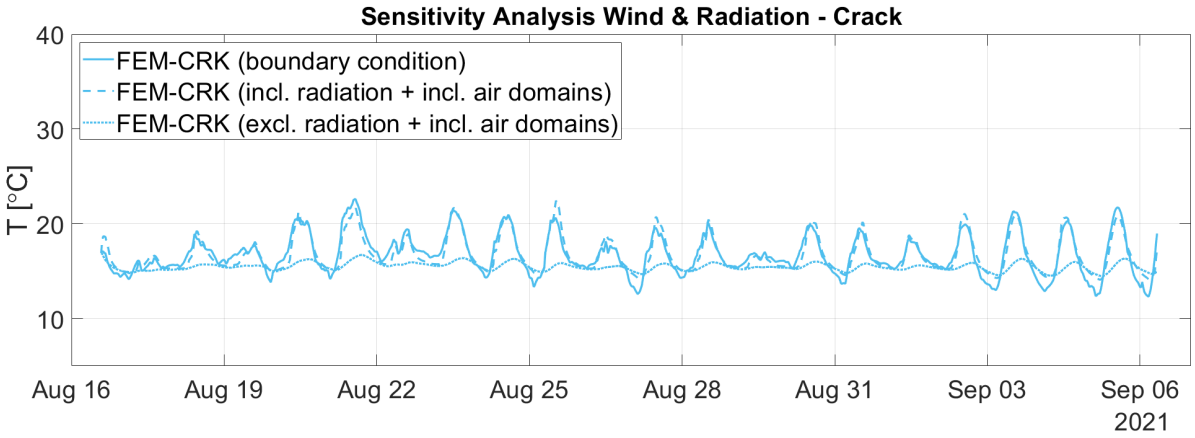

(a) Crack bottom.

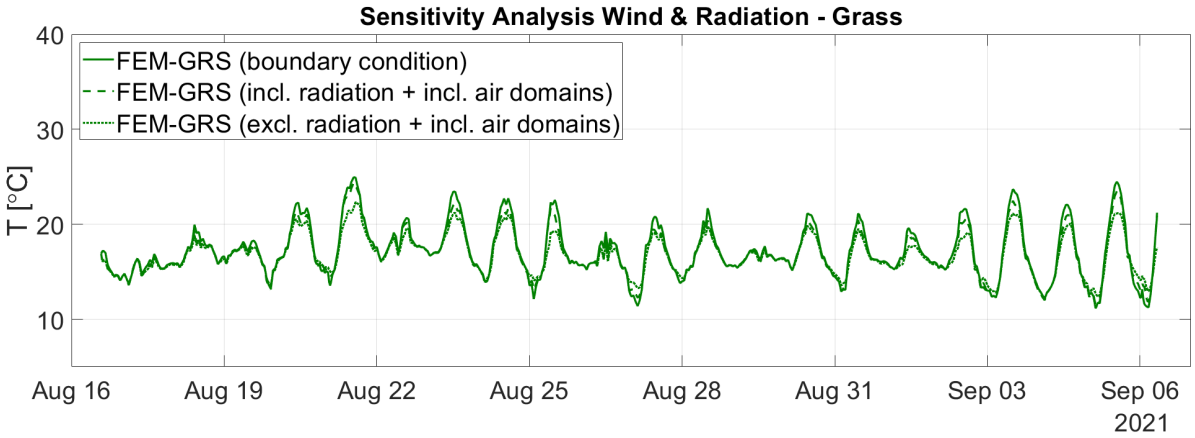

(b) Grass.

Figure 4.2: Thermal response in two different studies to determine the sensitivity of the model towards radiation and wind.

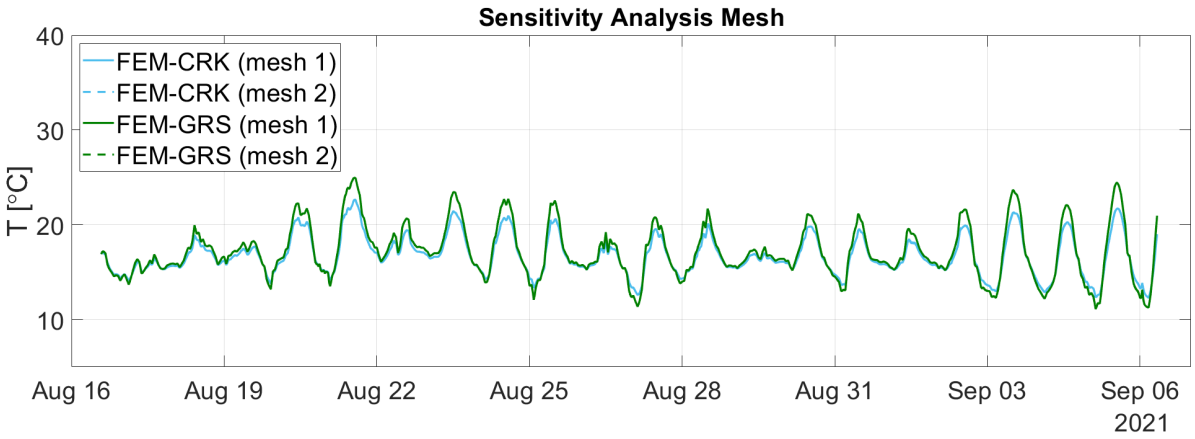

Figure 4.3: Thermal response in three different meshes to determine the sensitivity of the model towards a different mesh. The TRC time series of the crack, used for calibration, is added as an indication.

4.3. Sensitivity analysis of mesh and tolerance

Meshes can be identically physics-controlled, meaning that COMSOL finds the most optimal mesh for the geometry itself, or user-controlled. Using two meshes, the influence of the mesh structure on the thermal response of the bottom of the crack is investigated. Mesh 1 is shown in Figure D.3, having free tetrahedral elements for the cable and free quad for all remaining surfaces with a finer element size. Mesh 2 is physics-controlled with a course element size, containing warnings for a too-course mesh for the cable. So both meshes vary in element size. The tolerance was also varied in the hope of equal solution precision and less computation time, but this turned out to be negligible. The results of the mesh studies are shown in Figure 4.3. The influence of the meshes is negligible, and the crack and grass lines of different meshes are exactly the same. The computation time for the physics-controlled mesh was lower, but it contains warnings about elements having unconvenient sizes. The user-controlled mesh is preferred for modeling.

4.4. Calibration with TRC Images

Calibration is finished if the TRC data are comparable with the thermal data retrieved from the bottom of the modeled crack and grass points. The results are shown in Figure 4.4. The temperature response of FEM-GRS turned out to be more extreme (high maxima and low minima) than that of FEM-CRK on sunny, clear sky days.

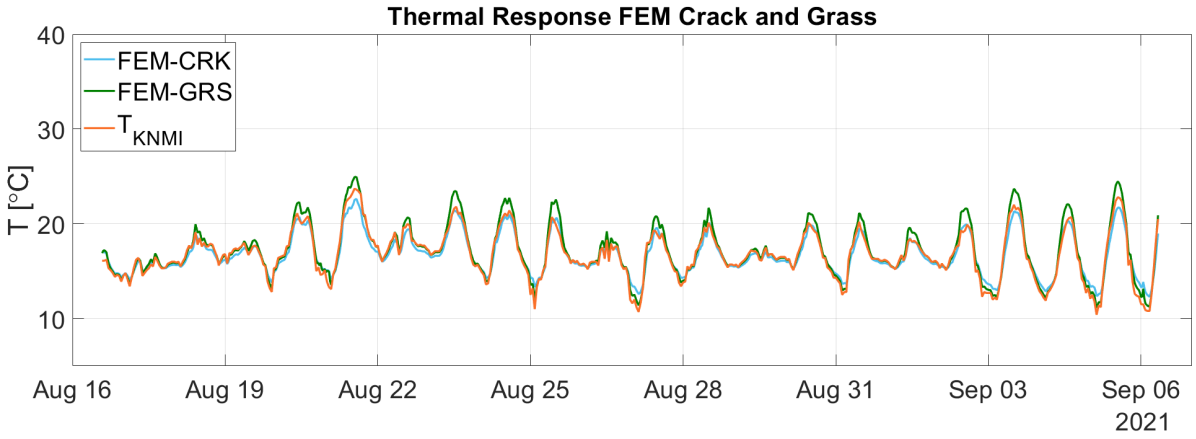

(a)

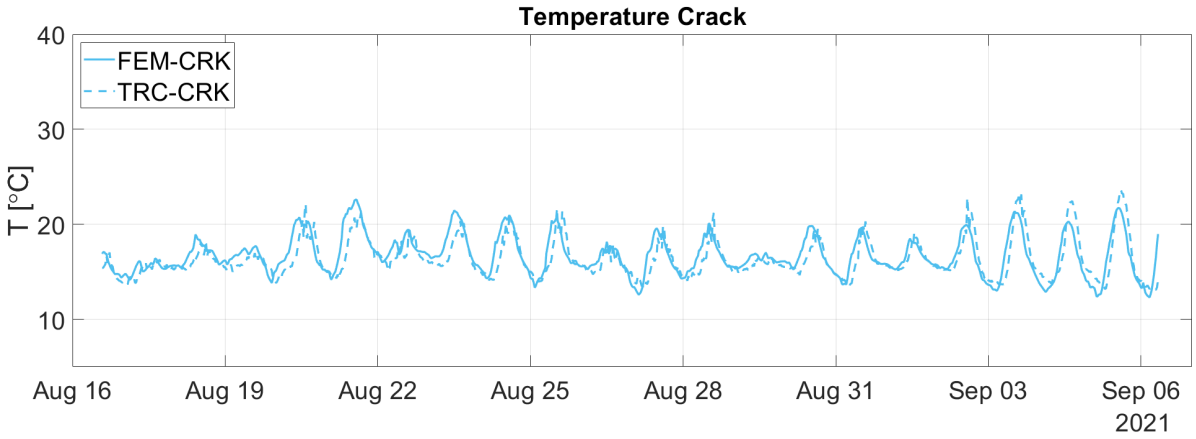

(b) Crack (bottom) point with relative error 6%.

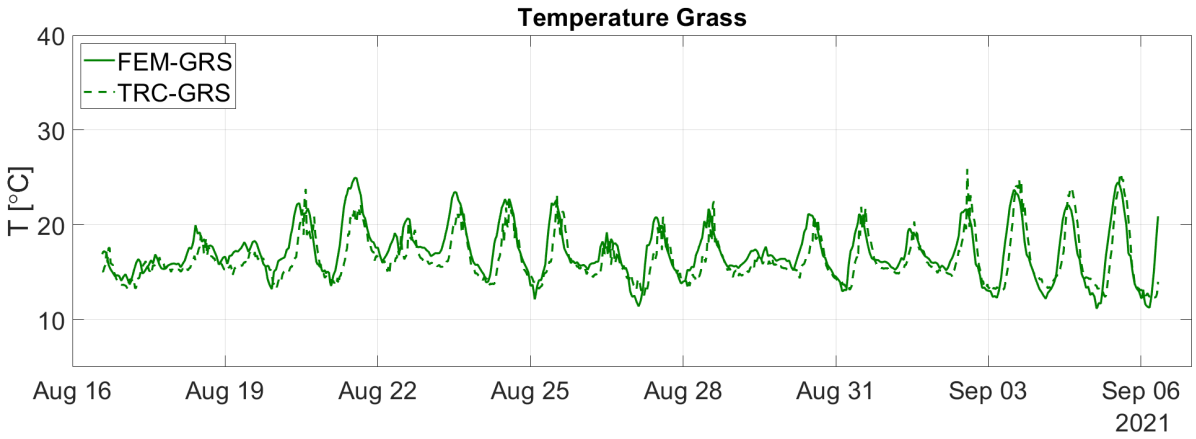

(c) Grass point with relative error 8%

Figure 4.4: Thermal response of modelled crack (bottom) and grass points compared to measured TRC images after calibration. At first sight there seems a lag between the FEM and TRC time series but after performing a cross-correlation analysis it turned out there is not.

5

Validation

What is the difference between the model and the experiment in terms of the thermal response of the cable?

After finishing the calibration, the validation, described in this chapter, can be started.

The outcome of the FEM model, shown in Figure 5.2, is being studied. During the day, FEM-CABCRK measures temperatures warmer than those of FEM-CABGRS. During the night, the reverse happens, and FEM-CABCRK is cooler than FEM-CABGRS. The thermal response of the FOS cable (represented by DTS data) shows the same. The lag in the DTS data (subsection 2.4.1)is already corrected in these figures. In combination with the TRC data used in chapter 4, a schematic overview of the thermal response of the system can be constructed, shown in Figure 5.1.

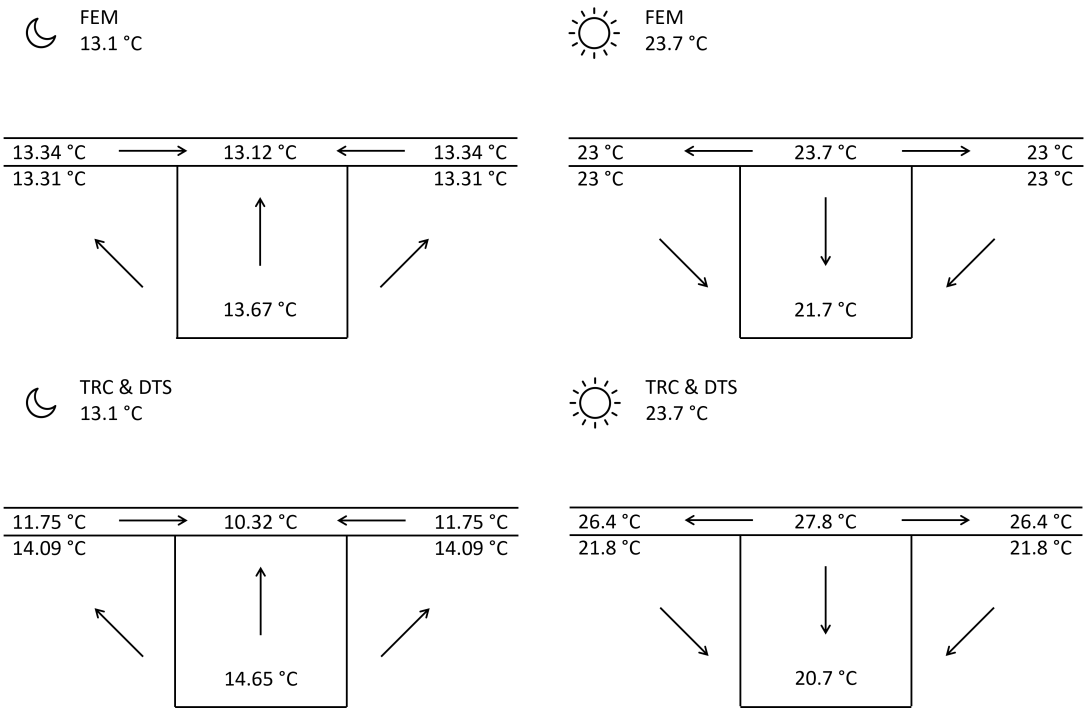

Figure 5.1: The thermal response of the system for August 21, 2021 02:30 and 13:30 with arrows indicating heat transport.

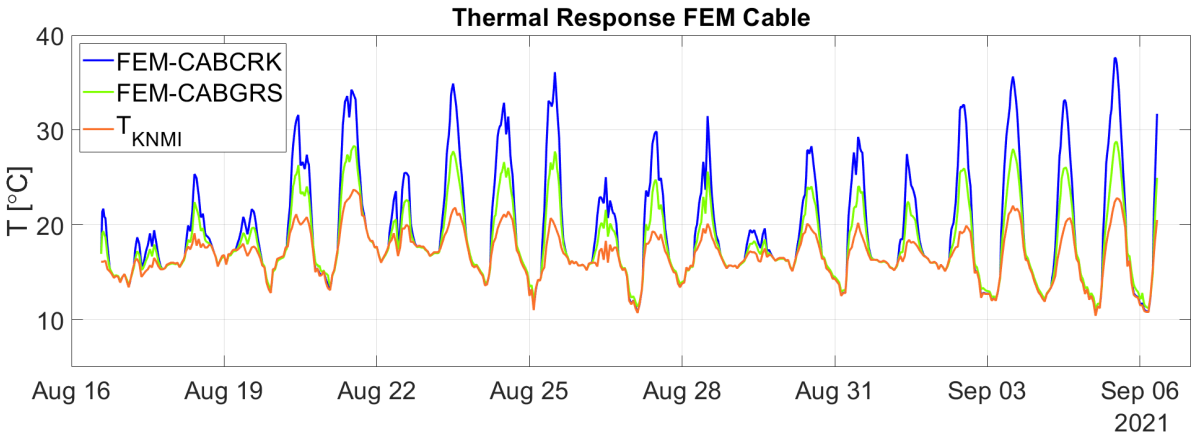

(a)

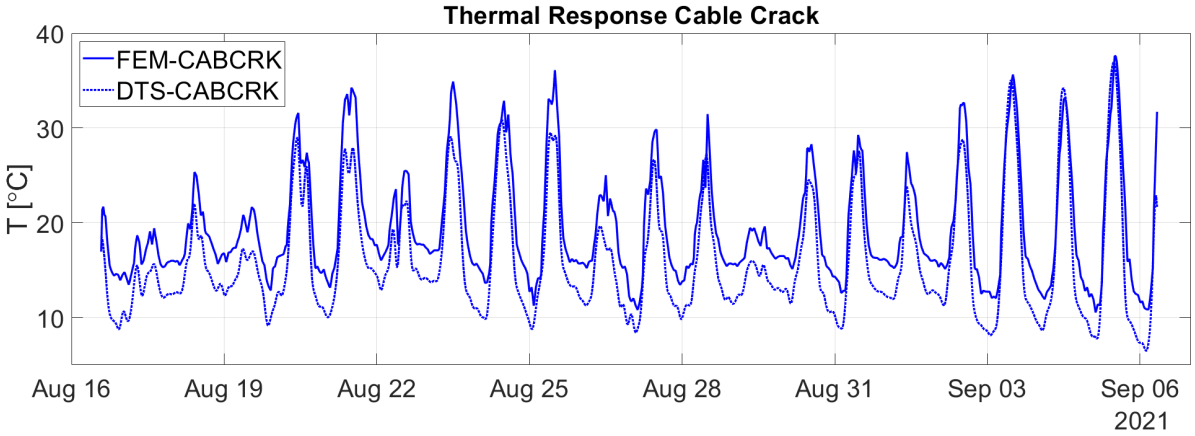

(b) Cable crack point with relative error 26%.

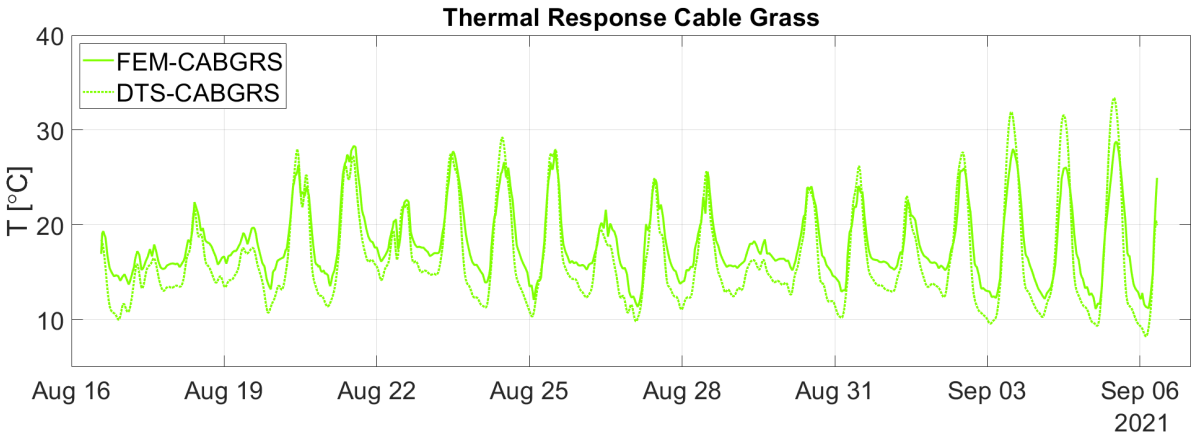

(c) Cable grass point with relative error 16%.

Figure 5.2: Thermal response of the cable crack and grass points for the FEM model compared with KNMI and DTS.

6

Influencing Conditions

Which conditions have a significant influence on the thermal response of a FOS cable based on the FEM outcome?

To see which conditions have a significant influence on the thermal response of the modeled cable, studies with changed model inputs are run, called scenarios. This chapter describes these scenarios. The results can be found back in Appendix F.

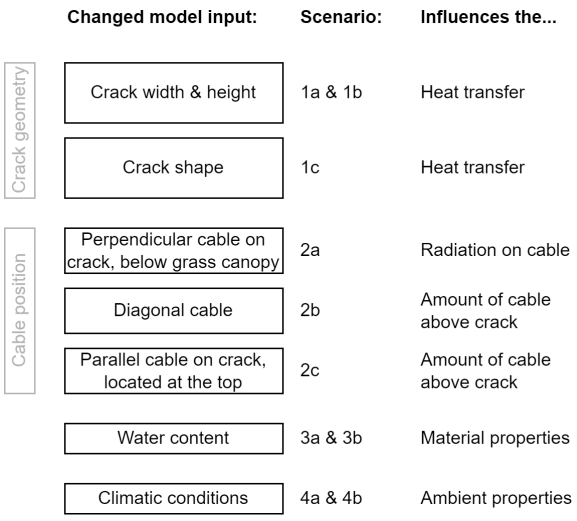

Figure 6.1: Performed studies to examine influencing conditions on the thermal response of the model.

The original width and height of the crack are based on the measured dimensions of the crack in Flood Proof Holland (Appendix A) $10cm$ and $17cm$, respectively. To test the influence of these dimensions on the thermal response of the cable, the model is run for a smaller crack ($1cm \times 1cm$) (**Scenario 1a**) and a larger crack ($100cm \times 100cm$) (**Scenario 1b**) in which the rest of the model conditions are kept the same (these dimensions are based on the observed crack sizes mentioned in section 2.1). In another study, a Y-shaped crack is created and modeled (like the one in FPH) to test the influence of the crack shape on the thermal response (**Scenario 1c**).

Crack detection may be more optimal if the cable is embedded in the soil and not exposed to radiation (**Scenario 2a**). In this way, only the cable in cracked regions is exposed, resulting in higher temperatures there. In addition to the influence of radiation, the influence of the amount of cable above the crack (cable-crack segment) is checked. The cable rotates with $45°C$ (**Scenario 2b**). The same can be done for a rotation of $90°C$ (**Scenario 2c**), having the cable parallel to the dike length, because cracks develop mostly parallel to the dike's length (section 2.1) (just like the crack at FPH).

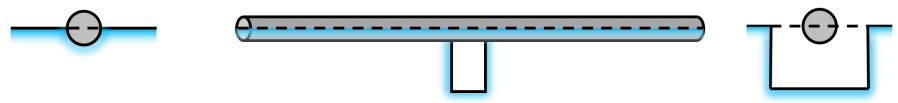

(a) Surfaces influenced by water content.

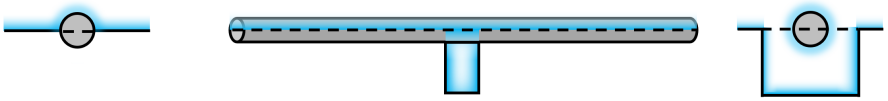

(b) Surfaces influenced by radiation and convection.

(c) Grass having a lower emissivity than the cable and peat.

Figure 6.2: Influences on the FOS cable, grass and crack system.

Since all materials are based on this time series and since the literature study shows that the water content is of great importance for crack development, this influence may be large (section 3.3 and section 3.4). To examine its influence, the water content (shown in Figure 3.8) is multiplied by 5 (**Scenario 3a**) and 0.5 (**Scenario 3b**) respectively.

The FEM model is currently calibrated and validated for a measurement period during summer 2021. To test how the model responds to other climatic conditions, KNMI data for two extreme climatic conditions are taken as input for the model. For both conditions, the data cover approximately one month: the heaviest storm (**Scenario 4a**), which was January 2018 [43] [44], and the hottest month (**Scenario 4b**), which was July 2019 [45]. For both scenarios, the lower soil layer is set to the average temperature of the period. Since the water content over time is not known for these periods, water contents of 0.5 and 0.2 are used for Scenario 4a and 4b respectively.

The FEM model results can be found in Appendix F. The animation shown in Figure 6.3a shows the thermal response of FEM-CABCRK for two different crack widths (Scenario 1). The same is done for A_{ptp} in Figure 6.3b.

(a) T.

(b) A_{ptp}.

Figure 6.3: Thermal response of FEM-CABCRK for two different crack widths (Scenario 1).

7

Crack Detection Model

What is the most optimal way to detect cracks using a FOS cable?

With the results of chapter 5 and chapter 6, the most optimal way to detect cracks using DTS can be found, based on studies for which the thermal difference between (CAB)CRK and (CAB)GRS is the biggest.

With a regression analysis, the relationship between the ambient KNMI properties and the modeled or observed FEM, DTS and TRC data is sought to be found. Regression lines are fitted using the least-squares method. The least squares method is the curve ($y = ax + b$) that best fits a set of observations with a minimum sum of squared errors, using vertical offset as the error between a data point and the fitted line.

$$a = \frac{n\sum xy - \sum y \sum x}{n\sum x^2 - (\sum x)^2} \tag{7.1}$$

$$b = \frac{\sum y - a\sum x}{n} \tag{7.2}$$

The best regression lines were found using the daily peak-to-peak temperature amplitude. Plots were made for the FEM, DTS and TRC data, respectively, and for the final FEM model (as explained in section 3.2) and Scenario 3a (higher water content). These can be found in Figure 7.2. Combining the 95% confidence bounds of these regression plots in Figure 7.1, only one measured diurnal time series and one diurnal air temperature time series are needed to detect a crack. To find the actual thermal response of the system after this, the DTS thermal response must be corrected for radiation overestimation. This approach can be found in Appendix G.

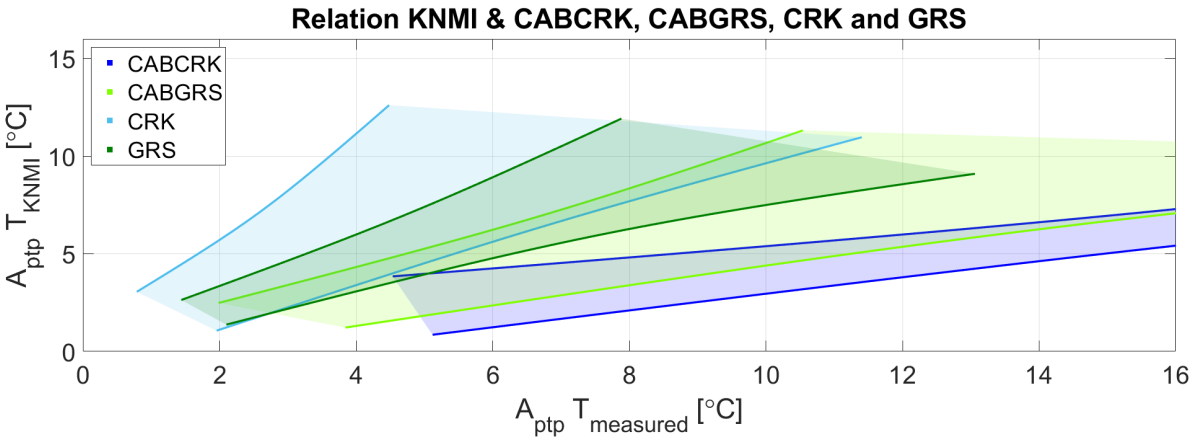

Figure 7.1: Domains based on 95% confidence bounds of all data sets shown in Figure 7.2.

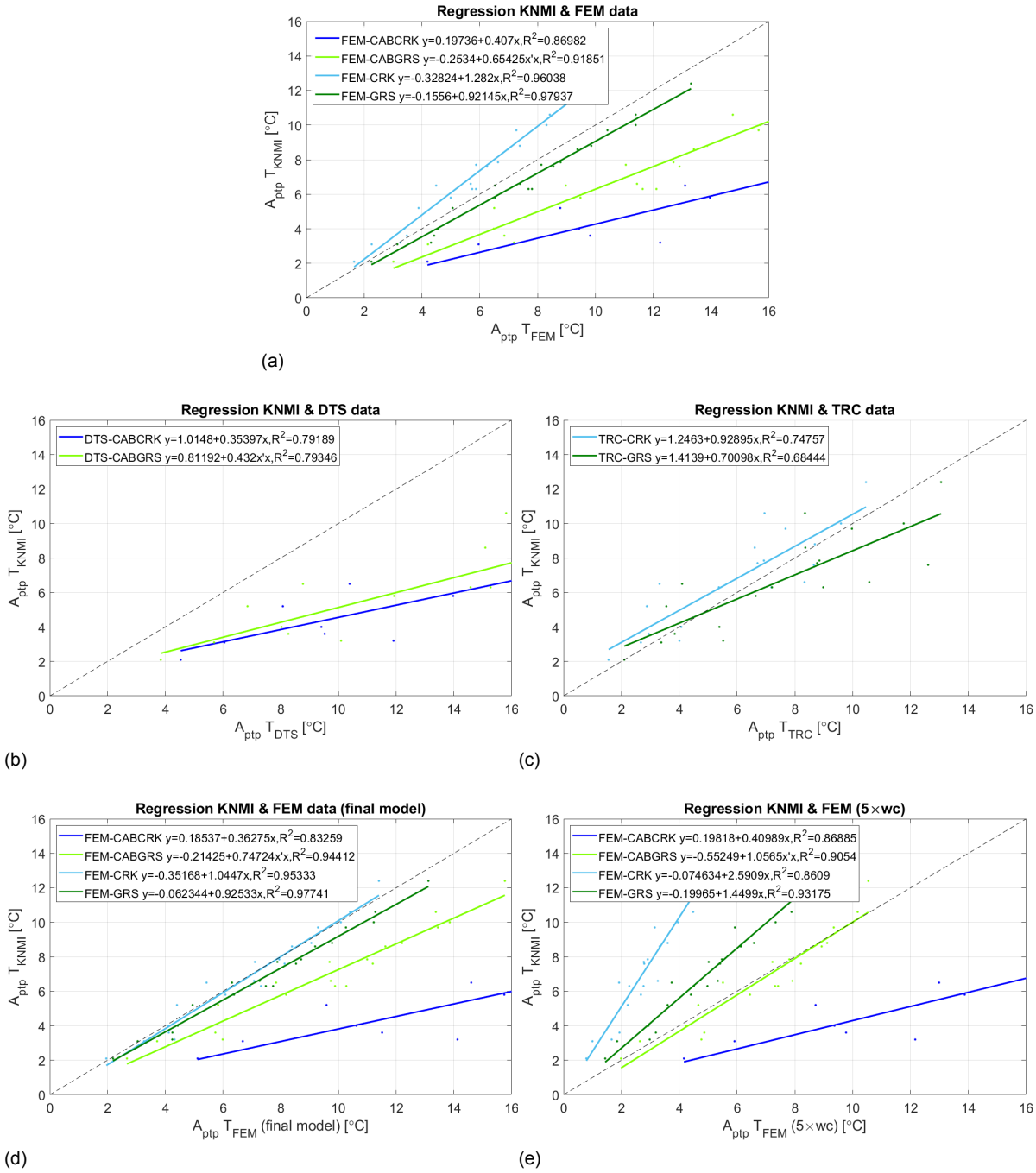

Figure 7.2: Regression plots (various data sets). The plot for DTS is using obtained time series, not corrected for radiation, but corrected for the lag in time as described in section 2.4.

8

Discussion

This chapter describes the interpretation of the research results and integrates these findings with early research work. It concludes which processes have major influence on the thermal response of the system and proposes three crack detection methods using DTS. Every research contains uncertainty regarding the approach performed and assumptions made, especially when constructing a model. At the end of this chapter, these points are briefly highlighted.

8.1. Crack Detection using DTS

Regular dike inspections occur during spring, when the storm season is over and most cracks are formed. Extra inspections are needed between April and September during the development of desiccated cracks [46], mainly when the precipitation deficit is greater than $175mm$ [9]. Therefore, most inspections occur in periods with low water content and relatively high radiation. This research concluded better crack detection using DTS on days with high radiation also. The thermal responses (lines in Figure B.4, section 4.1 and Figure 5.2) between grass and cracked domains are better distinguishable on sunny, uncloudy, dry days. Therefore, cracks are best detectable via DTS during the day (most of the time between 9:00 and 16:00) and when the cable is shaded, for example by implementing it below the grass canopy. In that way only cracked parts are prone to radiation (section 4.2 and chapter 6).

The cable is highly sensitive to its emissivity and embeddedness (section 4.2). This is most likely related to the cable covered with grass leaves and embedded in the soil in some parts, as can also be seen in Figure A.3.

Figure 5.1 shows the heat transport in the cable-crack system. This figure turned out to be valid for another summer month (July 2019), but differs for January 2018. Figure F.9 shows the results of the model during this winter. The response is not as sinusoidal regular as during the summer, but there are still several distinguishable peaks. These do not come from precipitation, but occurred on days when the air temperature varied a lot and the ground started acting as a buffer, tempering the thermal response of the grass domain. The water content was assumed to be 0.5 (higher than during the summer), increasing the buffering function of grass and peat. The thermal response of the crack domain on the other hand is almost completely following the air temperature, as it is not directly affected by the subsoil (Figure F.9). It is expected that when taking measurements in winter, when the time series of the system differ compared to summer due to the lack of radiation, the method explained in this research will be less straightforward. Therefore, when taking measurements during periods with less regular sinusoidal air temperatures such as winter months, one should be aware of these irregularities. The FEM-CABCRK point does follow the air temperature almost completely, implying when using a DTS thermal responses of cracked domains, in comparison with grass domains, follow the air temperature better.

Different crack geometries do not necessarily vary the thermal responses in the FEM model. The animation shown in Figure 6.3 shows the thermal response of FEM-CABCRK for two different crack widths. The area influenced by the crack can be clearly seen and is approximately twice the crack width. Considering that DTS uses the average thermal response of $25cm$ of the FOS cable (subsection 2.4.1),

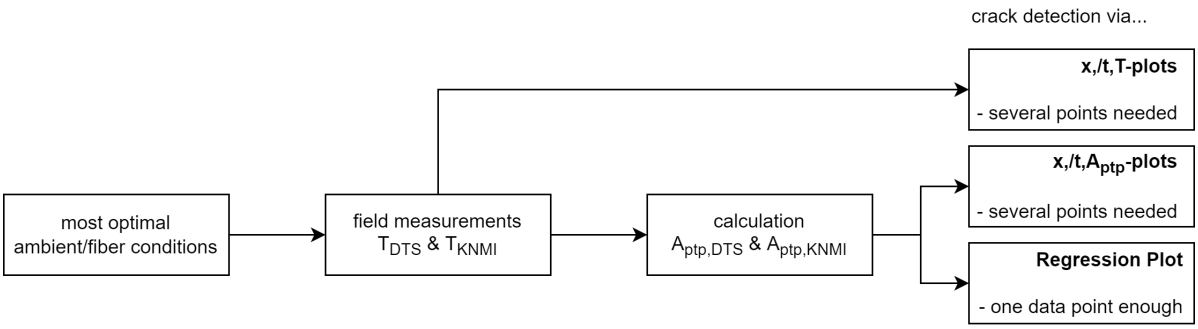

Figure 8.1: Three options for crack detection.

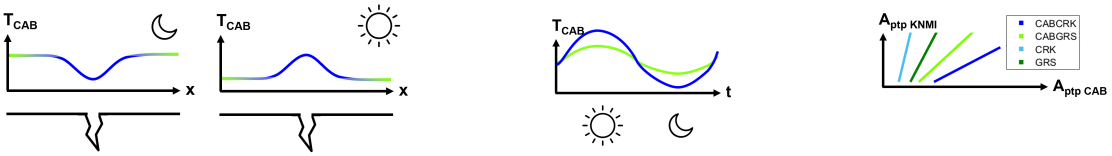

(a) x,T-plot (b) t,T-plot (c) Regression plot

Figure 8.2: Three methods for crack detection with DTS. NB: these are not uncorrected for radiation overestimation on the cable.

a larger cable-crack segment results in better crack detection: i.e. wider cracks, longer cable-crack segments, and multiple cracks in a range of $25cm$ (Y-shaped crack) give a better thermal response in the crack domain. The cable should be positioned parallel to the dike's length to ensure maximum cable-crack segment since cracks develop mostly parallel to the length of the dike (subsection 2.2.2).

As found in chapter 6 Scenario 3a, increasing the water content results in more distinguishable time series between crack and grass, so crack detection appears to be more effective for soils with a high water content. This is in line with can be concluded from chapter 7 Scenario 3a shown in Figure 7.2e, having the regression lines spread more. The reason for this is probably the difference in material properties of air and soil due to the higher water content influencing the soil, resulting in significantly deviant lines of crack and grass domains.

Finally, this research provides three ways to detect cracks using DTS information (Figure 8.1). The following subsections describe these crack detection methods. The black color of the cable results in an overestimation of the thermal response of the cable's outcomes. To find the actual thermal response of the cable-crack system, the measured DTS information needs to be corrected after the crack is detected. Several studies describe how this overestimation can be corrected for [47] [48], but none of them uses a FEM model. Here, regression graphs between radiation ($Q(t)$) and cable temperature ($T_{CAB}(t)$) are used, obtained from two FEM studies: including and excluding radiation on the cable. Taking the difference between those regression plots gives the overestimation of the cable due to radiation. More information about this correction can be found in Appendix G.

8.1.1. Crack detection with a x,T- or x,A_{ptp}-plot

Crack or grass domains can be visually found when observing measured time series. An example is shown in Figure 6.3 for which the thermal response at one moment in time is constant for the entire length of the cable, except for cracked locations. During nights, cracks are colder than grass. During the day it is the other way around. The x,T-plot for DTS data is shown in Figure 8.2a.

8.1.2. Crack detection with a t,T-plot

Another way of processing the DTS data is by making thermal plots over time. Cracks can be found using the line positions of the DTS time series (uncorrected for radiation, corrected for time lag) shown in Figure 8.2b.

8.1.3. Crack detection with a Regression Plot (Figure 7.1)

A more automated way of crack detection may be with regression plots shown in Figure 8.2c. The relation between the A_{ptp} of air and the A_{ptp} of cable is plotted. Regression plots between air and soil temperature were made before [49] [50], but regression plots with A_{ptp} have not been found in the literature so far. The advantage of using daily A_{ptp} is that it quantifies the heat storage in the system. During the day, the system charges: a high daily peak indicates high heat storage. The reverse happens at night: the system releases heat. Great temperature peaks and troughs indicate sensitivity to temperature changes and therefore more heat storage and release. Those systems/materials/domains have lower slopes in the regression plots.

Another advantage of A_{ptp} is that every point in the regression graph is a day. Days when less heat was added to the system (for example, cloudy and rainy days) are located in the lower regions, indicating an increase in heat storage according to Equation 3.5. Moving to higher A_{ptp} values on the line, the regression lines spread more, resulting in better crack detection, but more data from several studies (winter/summer, small/big crack, high/low wc and big/small cable embeddedness) have to be implemented to make the method more robust.

According to the TRC data described in chapter 4, CRK stores more heat than GRS. According to the DTS data described in chapter 5, CABCRK stores less heat than CABGRS. Figure 7.2 shows these differences too indicated by the position of the lines. Apparently, the amount of heat storage can be found back in the slope and position of the lines in the regression plots.

Another usage of the regression lines for crack detection is by taking daily A_{ptp}s of several locations in the cable, plot them in the regression plot, and see which of these points differ from the linear regression line fitted to them. The hypothesis is that a cracked spot will vary from the linear relationship between the daily A_{ptp} of air and the cable's formed by the points.

8.2. Data uncertainties

From chapter 6 it is found that the influence of the water content in the FEM model was high. It is therefore of importance to have a detailed water content during the measuring period to have a sufficient model calibration. Webcam images were used for determining the water content in the dike by using a relation between the grass greenness (from daylight images) and the water content. The brightness of every image is taken and therefore a constant light source is necessary, but the Sun is not. It disappears every night and during the day its intensity is changing constantly. Regarding the tools and data sets available for this research, the approach used was the most detailed and the graph of Figure 3.8 the closest to reality as possible. The technique was used in researches before [14] [51]. Nevertheless, the water content time series is in fact only trustworthy during the afternoon, when the sun is at its maximum capacity.

Secondly, the FPH dike contained little peat hills on top of the crack (Appendix A), causing uncertainty in the crack domain time series of the TRC images. During calibration, this time series is compared with the FEM crack point laying on the bottom of the FEM crack, which, due to differences in geometry, might be a questionable comparison. The small hills on top of the crack are warmed up more easily. It may be a straightforward assumption to compare their TRC thermal response with the crack bottom temperature of the FEM model.

Third, question marks can be placed on the DTS data. Figure 5.2 shows that the FOS cable measures colder temperatures during the night than the air temperatures measured by KNMI. During nights, the FEM model did not become cooler than the KNMI temperature, while the FOS cable in the field measured lower temperatures. During the afternoon, the cable observed much higher temperatures than the measured air temperature by KNMI. This can have several reasons, but most probable the calibration of the FOS cable in the field was not detailed enough. This calibration was done using a temperature TD diver placed in a cold bath (section 2.4). Another thought was the cable measuring the heat index instead of air temperature, but Appendix E proves not.

Furthermore, this research concluded that the FOS cable is highly sensitive to its embeddedness and radiation, but a grass canopy is never constant in space. Burned spots or high leaf densities can significantly influence the thermal response of the cable and therefore the measured DTS data.

Lastly, some of the webcam, TRC and DTS data contained noise caused by animals, for example animals moving the cable.

8.3. FEM model uncertainties

The FEM model is based on a heat balance equation (Equation 3.10). In this way, the influence of water transport is not accounted for. It is expected that it is an acceptable modeling choice for this research because the FEM thermal response turned out to be more or less the same as measured in the field and all major processes influencing heat fluxes in the boundary layer are accounted for (Figure 2.5). However, water transport is one of the mechanisms causing heat transfer (Figure 2.5) and therefore has an influence on the thermal response. Especially since the water content turned out to be an important influencing aspect of the thermal response of the system (Scenario 3a in chapter 6 and chapter 7).

The influence of air (wind, temperature and pressure) is added via a heat flux boundary condition. This boundary condition turned out to be a suitable approximation of the influence of these ambient properties if these do not vary rapidly over time. The same holds for the inner layers of the cable, which are currently not modeled since the ambient properties change slowly enough for these layers to anticipate. However, if one is interested in the turbulence or the air flow trajectories, a boundary condition cannot be applied anymore and the full air domain has to be included on top of the crack. Another remark that has to be placed by the use of a heat flux boundary condition is that it is currently applied to all surfaces exposed to air, having the same (forced) convection values over these surfaces (Equation 3.26). In reality, this assumption may not be completely true since (deep) cracks contain much smaller wind velocities compared to grass canopies and therefore experience less forced convection. In this research, the influence of modeling a separate air column on top of a crack is found to not give results that differ from using the heat flux boundary condition (Figure 4.2). However, one should be critical of implementing the ambient conditions in the form of a boundary condition.

9

Conclusion

Due to climate change, the thermal response of soils is changing. Especially for soils highly prone to drought, such as peat, the effects can be enormous. Desiccation cracks will develop more severely and more frequently. Currently, it is not possible to identify the exact location of cracks without having a human visual inspection, being less efficient in terms of kilometers inspected and highly prone to human errors. The purpose of this research was to develop a crack detection model by coupling FEM with measured TRC and DTS data and consequently to gain knowledge of the influences of the processes involved and eventually provide advice on the implementation of crack detection through DTS. This process has been completed successfully in the past months.

A FEM model is successfully developed, calibrated by thermal images, and validated by DTS data. It implies clarification regarding the most important processes involved when using the so-called DTS method for crack detection in dikes. The major drivers for the thermal response in the system turned out to be radiation and water content, in which a lot of radiation and a high water content result in more distinguishable thermal responses of crack and grass domains and therefore better crack detection. Several crack detection methods using DTS are given, detecting cracks in different shapes and positions. In x,T- and t,T-plots for sunny afternoons the FEM model and the DTS data (uncorrected for radiation) gave warmer T_{CABCRK} during the day and colder T_{CABCRK} during the night compared to T_{CABGRS}. In other words: a higher diurnal peak-to-peak temperature amplitude for cracks. Most probable will the T_{CABCRK} in winter months be more comparable with the air temperature compared to T_{CABGRS}, but this is not proved by measured data yet. A regression plot with on the y axis the peak-to-peak temperature amplitude of the air and on the x axis the peak-to-peak temperature amplitude of the cable implies another method, where only one measured time series is sufficient to detect crack presence. The standard position of the lines in the regression plot indicate that the FOS cable on cracked parts is warmer than on grass parts, heated up by radiation more. A lower slope means therefore more heat absorption compared to higher slopes in the regression plot. Radiation has the most influence on the cable in cracked parts, resulting in the best crack detection but an overestimation of the DTS data in those parts. A method to correct for radiation overestimation has been developed which can be consulted after crack detection to find the actual thermal response of the system without the overestimating influence of radiation on the black cable.

More research is desirable, especially the influence of radiation and the cooling function of water transport in the soil are not treated in this study. The hypothesis is that after more detailed research and better calibration and validation, this method can be implemented in the field as a measurement and forecasting device. It is expected that with accurate but especially longer periods and varying ambient conditions in field measurements, better regression plots may be found resulting in a method applicable to multiple situations.

The final FEM model, constructed in this Master thesis, forms a proper basis for future research on crack detection and forecasting through DTS. The FEM model is characterized by a cable embeddedness of 95% and emissivity as shown in Table 3.1. The material properties shown in Figure D.2 can be used, but when it is preferred to model the water transport in the system these domains have to be modeled as porous. Crack detection works best for maximum cable-crack segments and as cracks develop mainly parallel to the dike length the FOS cable should preferably be placed as such too.

10

Recommendations

This section elaborates some topics on which future research could look further into.

This report shows one way how peat and grass can be successfully modeled as a solid domain with a varying water content while having no water transport included. However, detailed information on how and where heat and water transport is not being investigated, while the water content turned out to be very important in determining the thermal response of the system (chapter 6 and section 8.1). Modeling both peat and grass domains as porous provides space to include these transport processes in the model. For this, the advice is to measure the grass leave density, the grass height, the emissivity, and material properties in the field as well. Measurements taken by Fugro Geoservices B.V. [4] of the peat soil at FPH already contain enough information to construct the porous peat domain, however, they do not change with time. Ideally, all the dependent parameters for determining the material properties, or even the material properties themselves, should be measured over time.

The lack of correct time series is not an issue for material properties alone, but also for the calibration (TRC) and validation (DTS) data. These were obtained during summer 2021, making it difficult to make predictions about the processes and the reliability of the model in winter. The method may be too simplified to implement in other situations. Bigger data sets containing various climatic conditions (colder air temperatures, wetter subsoils, etc.) for a much longer period are preferred to check the consistency of the method in these months also.

As mentioned in the discussion, the water content is an important influencing factor for the thermal response of the system and webcam images were used in this study to estimate this water content. This technique is not recommended to use in future researches as it is highly biased by the Sun's intensity. As a recommendation, detailed measuring equipment is desired, such as a moisture sensor installed in the peat soil, solving the key issue of having an unstably retrieved water content time series due to the lack of usable webcam images.

This study focused on crack detection using a FOS cable, but also recognized that this technique contains some uncertainties with respect to radiation and water content. The cable is heated by radiation, and the water content influences the cable from below (Figure 6.2). Crack detection using a thermal camera attached to a drone may be a solution less influenced by these conditions. The thermal images used in this research show a visible cable width of 3 pixels, but these time series of the cable response were unstable. Lenses of thermal camera's are available in various sizes, being able to measure not only in a close distance, but also in a football field away [52]. Having a small crack width of $2cm$ and 256×320 pixels per image (section 2.4), one pixel must be at maximum $2mm$ to account for a crack width of at least 10 pixels, having thermal images with a total width of $640mm$, so letting the drone fly about $1m$ above the dike, zigzagging across the dike. In this way also the cable time series could be obtained by thermal images, having a bigger data set for validation and a better, easier crack detection method, but taking into account that drones can only fly for about 15 to 30 minutes [53] at an average speed of $20ms^{-1}$ [54], priced for $€5,000 - 10,000,-$ [55], this technique is more expensive than a FOS cable of about $€1.50/m$ without having a pilot. Another drawback of using drones is that it is unknown to which extent thermal camera's can detect grass-covered cracks. Therefore, it is most likely that DTS will be used on a large scale sooner than drones with a thermal camera.

Regarding the DTS data, the influence of the color of the cable or the height of the grass is not investigated. It is expected, as in the study of De Jong et al. [47], that a white cable will be less sensitive to radiation, giving more realistic thermal responses. Future research should include cable segments varying in color, embeddedness, and shadyness to try to quantify the influence of radiation in more detail. For waterboards using DTS, the advice is not to mow constantly, but to ensure that the cable is in the shade and embedded as much as possible. In this way, radiation influences the cable only in cracks, resulting in better crack detection.

To conclude, this report presents a well-functioning crack detection model and also provides a concrete basis for a forecast crack detection method that can be developed in the future by monitoring a developing crack (from a fully covering grass canopy to a cracked one). Consider, for example, the ARIMA algorithm. In this report, no further research has been done on this topic, but it probably would offer opportunities for future research into the detection of developing cracks using DTS. The algorithm filters a trend, for example daily, out of a time series based on previous data and recognizes if data deviates, so in other words: it can recognize if a crack is developing/present or not.

Bibliography

[1] Sally Thompson and Karen Daniels. “Convection-driven pattern formation in lawn grasses”. In: (Nov. 2009).

[2] D. Makmur. *Which has the higher specific heat?* 2019. URL: https://slideplayer.com/slide/16338974/.

[3] Neda Yaghoobian et al. “Modeling the Thermal Effects of Artificial Turf on the Urban Environment”. In: *Journal of Applied Meteorology and Climatology* 49.3 (2010), pp. 332–345. DOI: 10.1175/2009jamc2198.1.

[4] Fugro Geoservices B.V. *Verkenning uitbreidingsmogelijkheden Flood Proof Holland*. Tech. rep. 1214-0088-000. Apr. 2015.

[5] P. B. McNulty and S. Kennedy. “Density Measurements of Grass by Toluene Displacement and Air Comparison Pycnometry”. In: *Irish Journal of Agricultural Research* 21.1 (1982), pp. 75–83. ISSN: 05787483. URL: http://www.jstor.org/stable/25556019.

[6] Hans Middendorp. *Dijkdoorbraak in Wilnis in 2003*. June 2018. URL: https://nietbangvoorwater.info/dijkdoorbraak-in-wilnis-in-2003/.

[7] Utrecht University. *Wat is het risico op dijkdoorbraak bij droogte?* July 2018. URL: https://www.uu.nl/nieuws/wat-is-het-risico-op-dijkdoorbraak-bij-droogte.

[8] Wouter Jan Klerk et al. “Accuracy of visual inspection of flood defences”. In: *Structure and Infrastructure Engineering* (Nov. 2021). DOI: 10.1080/15732479.2021.2001543.

[9] Hans Klip. *Duidelijke verschillen bij inspecties waterschappen tijdens droogte*. May 2019. URL: https://www.h2owaternetwerk.nl/h2o-actueel/duidelijke-verschillen-bij-inspecties-waterschappen-tijdens-droogte.

[10] Chao-Sheng Tang et al. “Desiccation cracking of soils: A review of investigation approaches, underlying mechanisms, and influencing factors”. In: *Earth-Science Reviews* 216 (2021), p. 103586. ISSN: 0012-8252. DOI: https://doi.org/10.1016/j.earscirev.2021.103586. URL: https://www.sciencedirect.com/science/article/pii/S0012825221000866.

[11] Hitoshi Matsubara et al. “Numerical modelling of mudcrack growth”. In: *Japanese Geotechnical Society Special Publication* 2.31 (2016), pp. 1143–1147. DOI: 10.3208/jgssp.ATC1-3-17.

[12] Majid Sedighi et al. “Energy balance at the soil atmospheric interface”. In: *Environmental Geotechnics* 5.3 (2018), pp. 146–157. DOI: 10.1680/jenge.15.00054. eprint: https://doi.org/10.1680/jenge.15.00054. URL: https://doi.org/10.1680/jenge.15.00054.

[13] Luca Schenato et al. “Design and field testing of a fiber optic pressure sensor for underground water level monitoring”. In: *Seventh European Workshop on Optical Fibre Sensors*. Ed. by Kyriacos Kalli, Sinead O. O’Keeffe, and Gilberto Brambilla. Vol. 11199. International Society for Optics and Photonics. SPIE, 2019, pp. 93–96. DOI: 10.1117/12.2540812. URL: https://doi.org/10.1117/12.2540812.

[14] Lu et al. “Using UAV Visible Images to Estimate the Soil Moisture of Steppe”. In: *Water* 12.9 (2020). ISSN: 2073-4441. DOI: 10.3390/w12092334. URL: https://www.mdpi.com/2073-4441/12/9/2334.

[15] Wenhui Cui and Ting Fong May Chui. “Subsurface Lateral Heat Flux within the Heterogeneous Surface of a Subtropical Wetland and Its Potential Contribution to Energy Imbalance”. In: *Journal of Hydrometeorology* 18.12 (2017), pp. 3125–3144. DOI: 10.1175/JHM-D-17-0006.1. URL: https://journals.ametsoc.org/view/journals/hydr/18/12/jhm-d-17-0006_1.xml.

[16] Bense et al. “Using distributed temperature sensing to monitor field scale dynamics of ground surface temperature and related substrate heat flux”. In: *Agricultural and Forest Meteorology* 220 (2016), pp. 207–215. ISSN: 0168-1923. DOI: https://doi.org/10.1016/j.agrformet.2016.01.138. URL: https://www.sciencedirect.com/science/article/pii/S0168192316301496.

[17] Leonardo Duarte Campos and Juan Pablo Aguilar López. *CO Meeting Organizer EGU2*. Mar. 2021. URL: https://meetingorganizer.copernicus.org/EGU21/EGU21-14904.html.

[18] Chaosheng Tang et al. “Influencing factors of geometrical structure of surface shrinkage cracks in clayey soils”. In: *Engineering Geology* 101.3 (2008), pp. 204–217. ISSN: 0013-7952. DOI: https://doi.org/10.1016/j.enggeo.2008.05.005. URL: https://www.sciencedirect.com/science/article/pii/S0013795208001531.

[19] Chao-Sheng Tang et al. “Experimental characterization of shrinkage and desiccation cracking in thin clay layer”. In: *Applied Clay Science* 52.1 (2011), pp. 69–77. ISSN: 0169-1317. DOI: https://doi.org/10.1016/j.clay.2011.01.032. URL: https://www.sciencedirect.com/science/article/pii/S0169131711000536.

[20] Chao-Sheng Tang et al. “Experiment evidence on the temperature dependence of desiccation cracking behavior of clayey soils”. In: *Engineering Geology* 114.3 (2010), pp. 261–266. ISSN: 0013-7952. DOI: https://doi.org/10.1016/j.enggeo.2010.05.003. URL: https://www.sciencedirect.com/science/article/pii/S0013795210000773.

[21] North Carolina Climate Office. *Latent and Sensible Heat | North Carolina Climate Office*. URL: https://legacy.climate.ncsu.edu/edu/Heat.

[22] STOWA. *Stabiliteit veenkades*. URL: https://www.stowa.nl/deltafacts/waterveiligheid/waterveiligheidsbeleid-en-regelgeving/stabiliteit-veenkades.

[23] Ziyang Li et al. “Unsteady Seepage Behavior of an Earthfill Dam During Drought-Flood Cycles”. In: *Geosciences* 9.1 (2019). ISSN: 2076-3263. URL: https://www.mdpi.com/2076-3263/9/1/17.

[24] STOWA. *Stabiliteit van veenkaden tijdens droogte*. Tech. rep. 2004-37. 2004. URL: https://www.stowa.nl/sites/default/files/assets/PUBLICATIES/Publicaties%202000-2010/Publicaties%202000-2004/STOWA%202004-37.pdf.

[25] S. Baram et al. “Water percolation through a clayey vadose zone”. In: *Journal of Hydrology* 424-425 (2012), pp. 165–171. ISSN: 0022-1694. DOI: https://doi.org/10.1016/j.jhydrol.2011.12.040. URL: https://www.sciencedirect.com/science/article/pii/S0022169411009449.

[26] TU Delft. *Flood proof Holland*. URL: https://www.tudelft.nl/innovatie-impact/ontwikkeling-innovatie/innovation-projects/flood-proof-holland.

[27] fibrisTerre. *Technology*. URL: https://www.fibristerre.de/technology/.

[28] Peter R.N. Childs. Ed. by Peter R.N. Childs. Oxford, 2011. DOI: https://doi.org/10.1016/B978-0-12-382098-3.00002-0. URL: https://www.sciencedirect.com/science/article/pii/B9780123820983000020.

[29] Sen Lu et al. “An Improved Model for Predicting Soil Thermal Conductivity from Water Content at Room Temperature”. In: *Soil Science Society of America Journal* 71.1 (2007), pp. 8–14. DOI: https://doi.org/10.2136/sssaj2006.0041. eprint: https://acsess.onlinelibrary.wiley.com/doi/pdf/10.2136/sssaj2006.0041. URL: https://acsess.onlinelibrary.wiley.com/doi/abs/10.2136/sssaj2006.0041.

[30] Gaylon Campbell and John Norman. *An Introduction to Environmental Biophysics*. New York, Verenigde Staten: Springer Publishing, 2012. DOI: 10.1007/978-1-4612-1626-1.

[31] Arterra/Universal Images Group. *Peat extraction in bog showing piles of harvested peat drying to be used as traditional fuel.* May 2018. URL: https://www.gettyimages.nl/detail/nieuwsfoto%27s/peat-extraction-in-bog-moorland-showing-piles-of-nieuwsfotos/1141721466.

[32] Ying Zhao and Bingcheng Si. “Thermal properties of sandy and peat soils under unfrozen and frozen conditions”. In: *Soil and Tillage Research* 189 (2019), pp. 64–72. ISSN: 0167-1987. DOI: https://doi.org/10.1016/j.still.2018.12.026.

[33] Louis W. Dekker and Coen J. Ritsema. “Variation in water content and wetting patterns in Dutch water repellent peaty clay and clayey peat soils”. In: *CATENA* 28.1 (1996), pp. 89–105. ISSN: 0341-8162. DOI: https://doi.org/10.1016/S0341-8162(96)00047-1. URL: https://www.sciencedirect.com/science/article/pii/S0341816296000471.

[34] Van Hemert et al. *Onderzoek naar maatregelen voor versnelde herbevochtiging van verdroogde veenkaden en vertraagde verdroging van veenkaden*. Vol. juni. STOWA, 2006.

[35] Stuart W. Churchill. “A comprehensive correlating equation for forced convection from flat plates”. In: *AIChE Journal* 22.2 (1976), pp. 264–268. DOI: https://doi.org/10.1002/aic.690220207. eprint: https://aiche.onlinelibrary.wiley.com/doi/pdf/10.1002/aic.690220207. URL: https://aiche.onlinelibrary.wiley.com/doi/abs/10.1002/aic.690220207.

[36] J.W. Rose. “Boundary-layer flow on a flat plate”. In: *International Journal of Heat and Mass Transfer* 22.6 (1979), p. 969. ISSN: 0017-9310. DOI: https://doi.org/10.1016/0017-9310(79)90037-1. URL: https://www.sciencedirect.com/science/article/pii/0017931079900371.

[37] COMSOL. *Deriving the Radiative Heat Flux for Opaque Surfaces*. URL: https://doc.comsol.com/5.5/doc/com.comsol.help.heat/heat_ug_theory.07.36.html.

[38] Ministerie van Infrastructuur en Waterstaat. *dp1: Kwaliteitsgecontroleerde klimaatgegevens NL per uur, gestandaardiseerd datapakket*. Dec. 2021. URL: https://www.knmidata.nl/data-services/knmi-producten-overzicht/klimatologische-gegevens/data-product-1.

[39] Meng et al. “Estimating Land Surface Temperature from Feng Yun-3C/MERSI Data using a New Land Surface Emissivity Scheme”. In: *Remote Sensing* 9 (Dec. 2017). DOI: 10.3390/rs9121247.

[40] ThermoWorks. *Infrared Emissivity Table*. URL: https://www.thermoworks.com/emissivity-table/.

[41] Thompson et al. “Seasonal variation in albedo and radiation exchange between a burned and unburned forested peatland: implications for peatland evaporation”. In: *Hydrological Processes* 29.14 (2015), pp. 3227–3235. DOI: 10.1002/hyp.10436.

[42] Fanny Gerber et al. “Modeling directional–hemispherical reflectance and transmittance of fresh and dry leaves from 0.4µm to 5.7µm with the PROSPECT-VISIR model”. In: *Remote Sensing of Environment* 115 (Feb. 2011), pp. 404–414. DOI: 10.1016/j.rse.2010.09.011.

[43] Nederland voor beginners. *Het weer in Nederland*. May 2019. URL: https://www.nederlandvoorbeginners.info/weer-en-klimaat/#:%7E:text=Hoewel%20de%20herfst%20de%20reputatie,maart%20kennen%20redelijk%20hoge%20windsnelheden.

[44] Rico Schröder. *Komen zware stormen het vaakst in de herfst voor?* Sept. 2021. URL: https://www.weeronline.nl/nieuws/komen-zware-stormen-het-vaakst-in-de-herfst-voor.

[45] Vivian Lammerse. *De aarde heeft net de allerwarmste maand ooit gemeten achter de rug*. Aug. 2021. URL: https://scientias.nl/de-aarde-heeft-net-de-allerwarmste-maand-ooit-gemeten-achter-de-rug/#:%7E:text=In%202019%20stegen%20de%20temperaturen,de%20warmste%20maand%20ooit%20gemeten.

[46] *Dijkinspecties voor veilige waterkeringen*. URL: https://www.hhdelfland.nl/ontdekwerk/stevige-dijken/stormseizoen/dijkinspecties-veilige-waterkeringen/.

[47] De Jong et al. “Fiber optic distributed temperature sensing for the determination of air temperature”. In: *Atmospheric Measurement Techniques* 8.1 (2015), pp. 335–339. DOI: 10.5194/amt-8-335-2015. URL: https://amt.copernicus.org/articles/8/335/2015/.

[48] Bethany Neilson et al. “Effect of Solar Radiation on Fiber Optic Cables Used in Distributed Temperature Sensing (DTS) Applications”. In: *AGU Fall Meeting Abstracts* (Dec. 2008).

[49] Shiferaw Munie, Petr Madera, and Jindrich Pavlis. “Soil temperature in an open site and below two plantation forest canopies in a tropical highland area, southern Ethiopia”. In: *Theoretical and Applied Climatology* 139 (Feb. 2020). DOI: 10.1007/s00704-019-03031-3.

[50] D. Barman et al. “Soil temperature prediction from air temperature for alluvial soils in lower Indo-Gangetic plain”. Nederlands. In: *International Agrophysics* 31.1 (Jan. 1, 2017), pp. 9–22. DOI: 10.1515/intag-2016-0034. URL: http://dx.doi.org/10.1515/intag-2016-0034.

[51] Lim Eng et al. “The Use of VARI, GLI, and VIgreen Formulas in Detecting Vegetation In aerial Images”. In: *International Journal of Technology* 10 (Nov. 2019), p. 1385. DOI: 10.14716/ijtech.v10i7.3275.

[52] Connors Industrials Inc. *How Far Can You Measure With a Thermal Camera?* URL: https://connorsindustrials.com/far-can-measure-thermal-camera/.

[53] Jasper van der Vliet. *Hoelang kan een drone vliegen? - Verhoog je vliegtijd*. Sept. 2021. URL: https://drone-optiek.nl/hoelang-kan-een-drone-vliegen/#:%7E:text=Een%20drone%20kan%20ongeveer%20tussen,verkocht%20aan%20het%20grote%20publiek..

[54] SATIR. *SATIR Thermal Imaging UAV Drone System*. URL: https://satir.com/product/uav-drone-640p.

[55] ThermalCamera.Shop. *FLIR thermal imaging cameras for Drones*. URL: https://www.warmtebeeldcamer
nl/en/thermal-cameras/drone/.

[56] P. Buitendijk. *Demonstratie terrein Tijdelijke Waterkeringen*. Tech. rep. 993708. Nov. 2013.

[57] COMSOL. *Understanding, and changing, the element order - Knowledge Base*. URL: https://www.comsol.com/support/knowledgebase/1270#:%7E:text=Fluid%20Flow,-The%20default%20for&text=Linear%20shape%20functions%20are%20used,are%20used%20for%20the%20pressure..

[58] Wikipedia contributors. *Heat index*. July 2022. URL: https://en.wikipedia.org/wiki/Heat_index.

A

Dike and Crack Specifications

Figure A.2: Fiber optic sensor cable. The crack is shown in cyan.

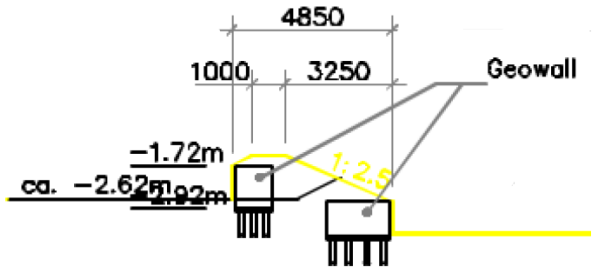

Figure A.1: Flood Proof Holland dike dimensions by BAM Infraconsult bv in mm. [56]

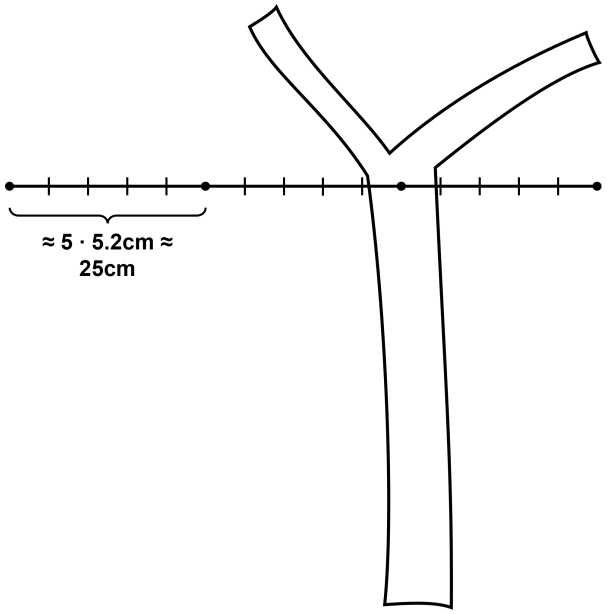

Figure A.4: Top view of segments used by DTS to generate the thermal response data of every $25cm$.

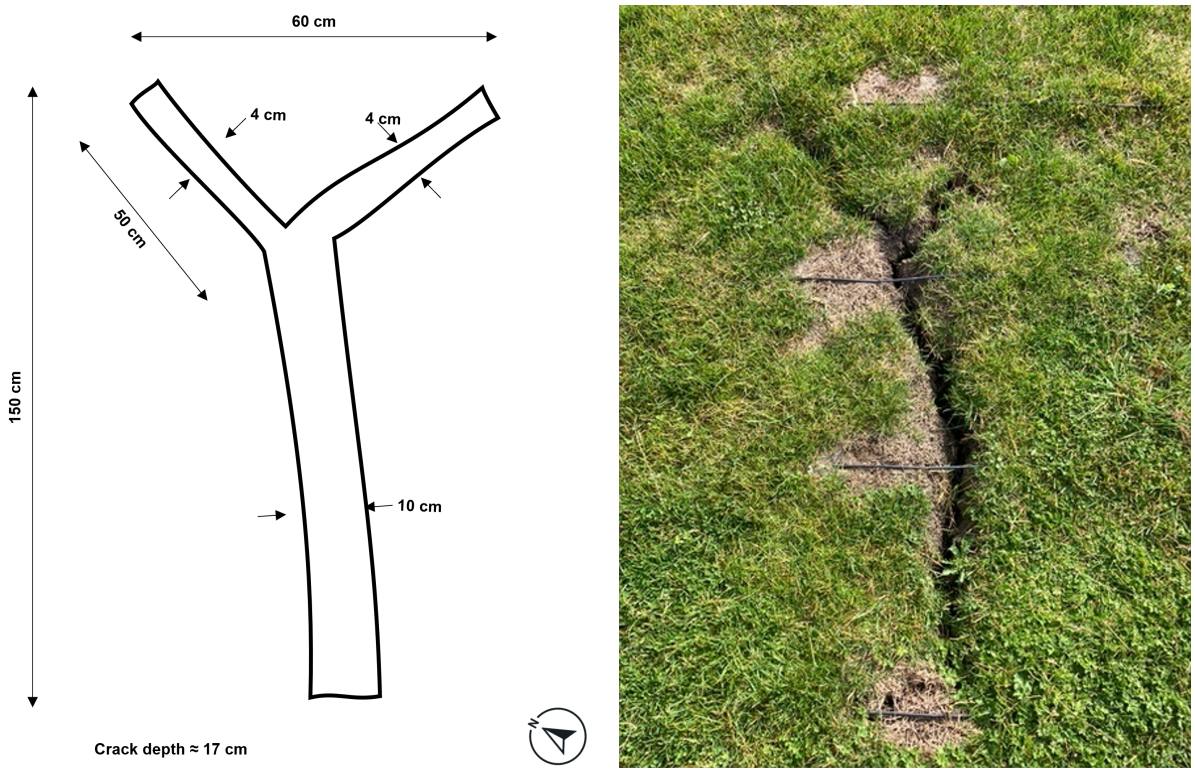

Figure A.3: Flood Proof Holland crack dimensions.

B

Data Time Series

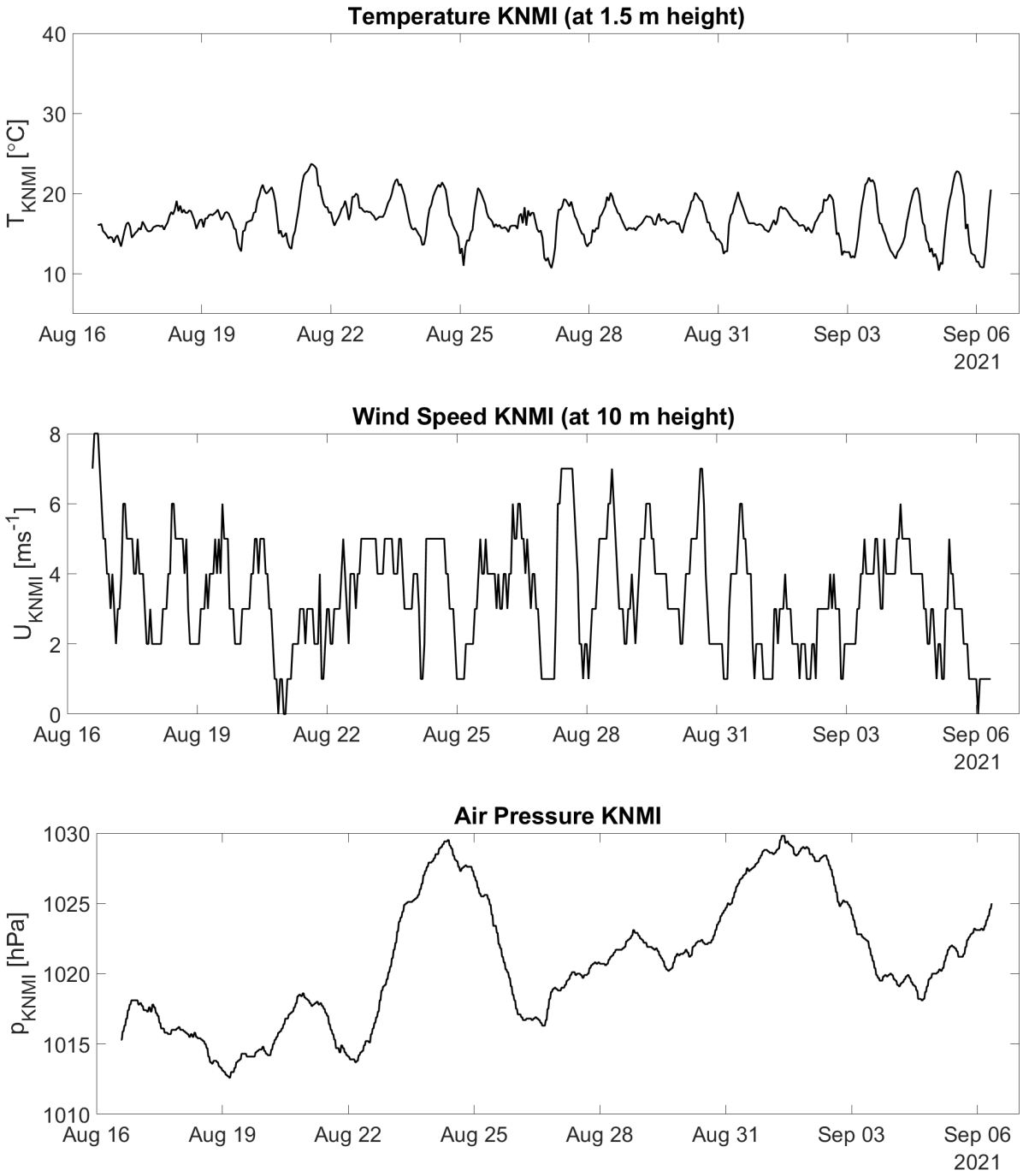

Figure B.1: KNMI data.

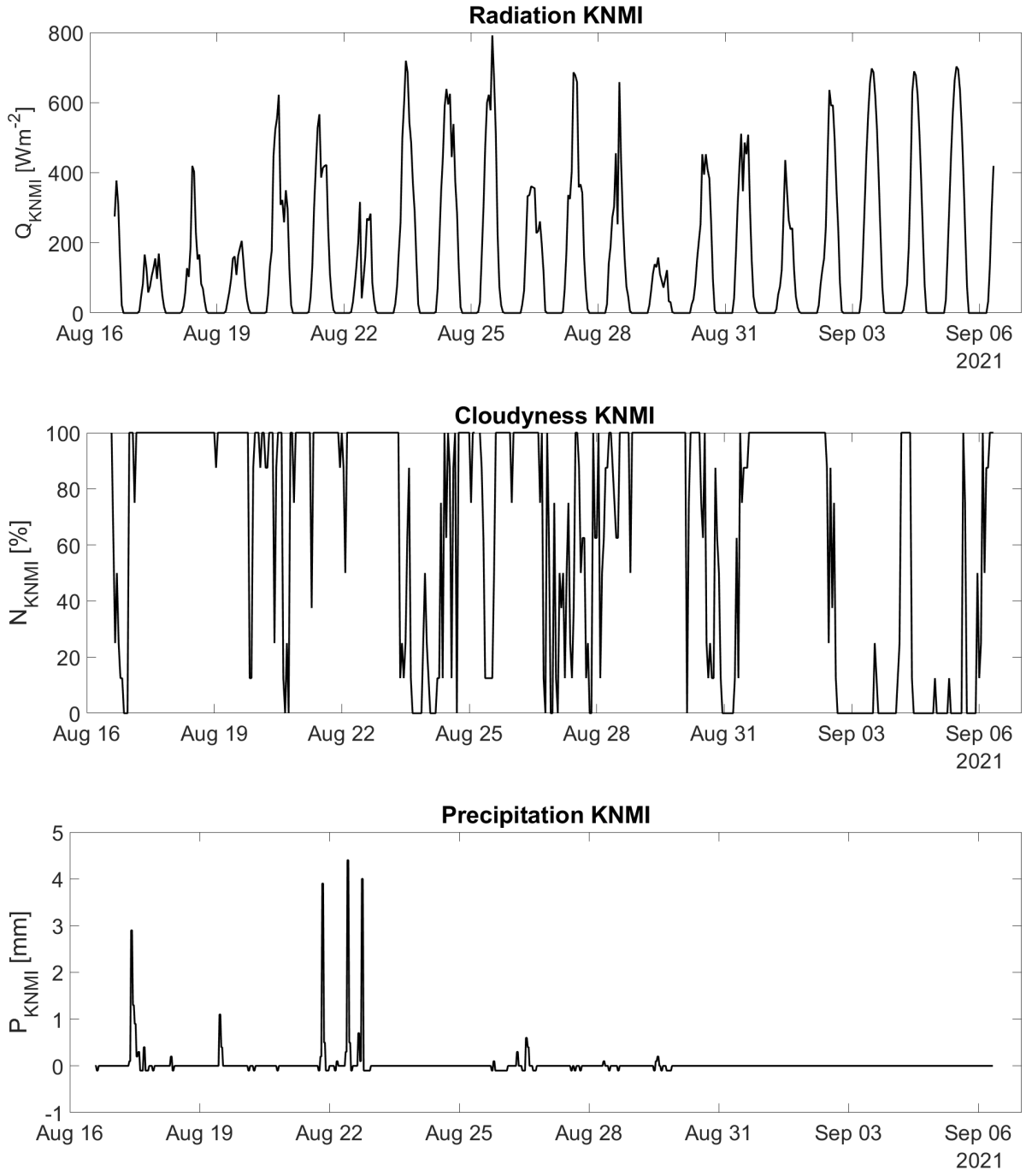

Figure B.2: KNMI data.

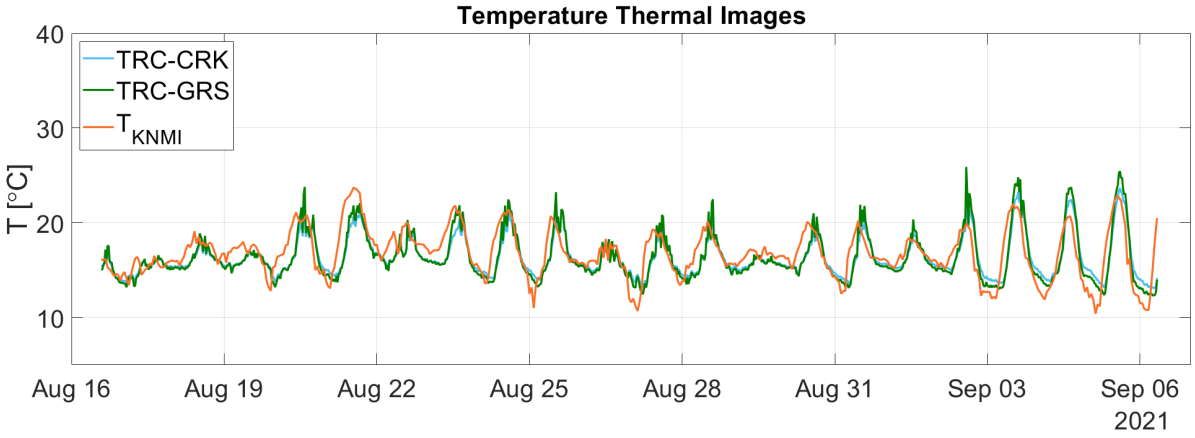

Figure B.3: Measured TRC temperature data.

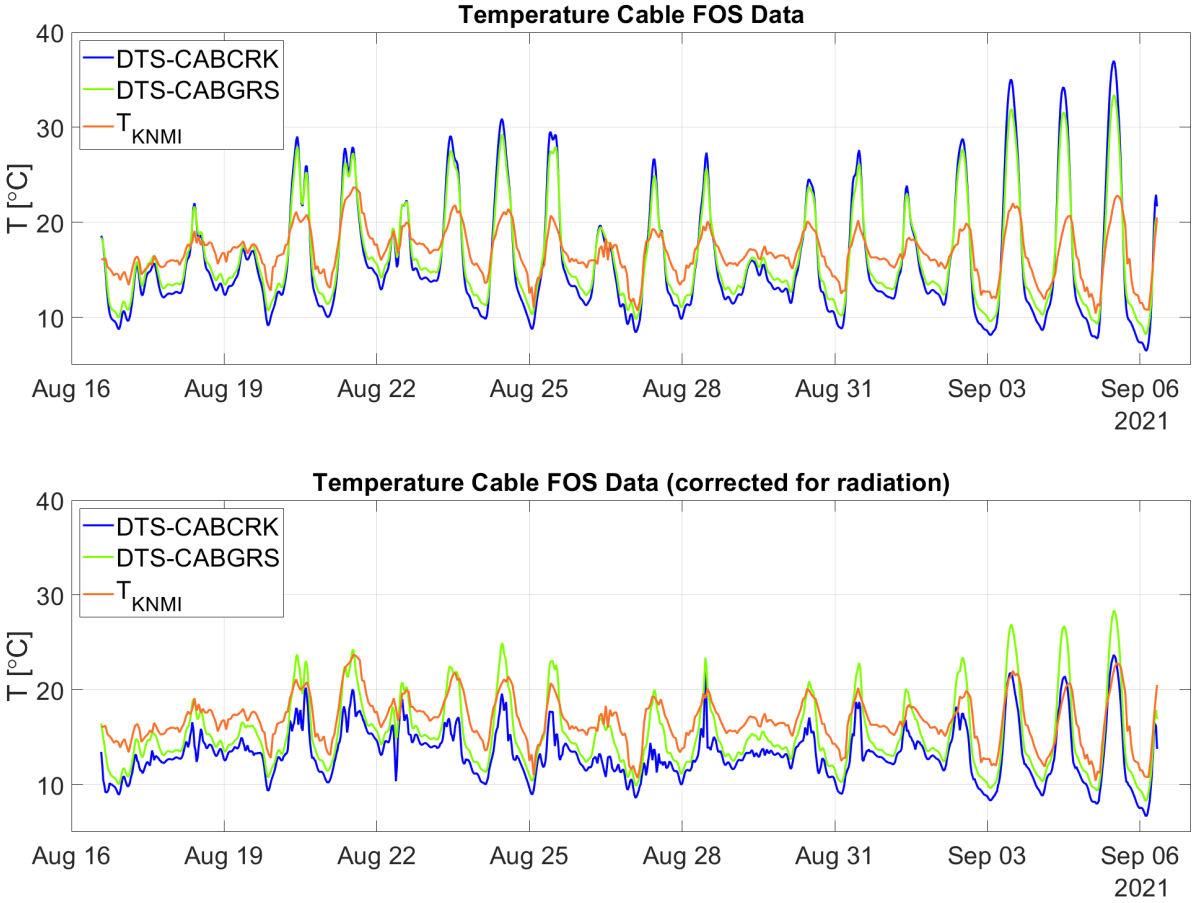

Figure B.4: Measured and corrected DTS temperature data.

C

Finite Element Method

Space- and time-dependent problems are usually expressed in terms of a Partial Differential Equation (PDE). When a differential equation is expressed in terms of the derivatives of more than one independent variable (for example t, x, y and z), it is referred to as a PDE. In the example of Equation C.1 u is the dependent variable and x and y are independent variables.

$$\frac{\partial^2 u}{\partial x^2} + \frac{\partial^2 u}{\partial y^2} = 0 \tag{C.1}$$

Most of the PDE-problems cannot be solved with analytical methods to find the value of the dependent variables at different times and positions. The Finite Element Method (FEM) solves these problems by approximating the solutions to the PDEs with numerical model equations, which can be solved using numerical methods. This process is called discretisation. The solution to the numerical model equations are, in turn, an approximation of the real solution to the PDEs. The Galerkin method – one of the many possible FEM-formulations – can be used for discretisation.

For complex systems with more couplings between equations, finding the solutions is not as straightforward. One of these problems is given in the example beneath.

FEM Example

$$\rho C_p \frac{\partial T}{\partial t} + \nabla \cdot (-k \nabla T) = g(T, t, \underline{x}) \tag{C.2}$$

Assume that the temperature distribution in a heat sink is being studied, given by Equation C.2, but now at steady state, meaning that the time derivative of the temperature field in Equation C.2 is zero. The equation for the model domain Ω becomes the following:

$$\nabla \cdot (-k \nabla T) = g(T, \underline{x}) \text{ in } \Omega \tag{C.3}$$

Further, assume that the temperature along a boundary ($\partial\Omega_1$) is known, in addition to the expression for the heat flux normal to some other boundaries ($\partial\Omega_2$). On the remaining boundaries, the heat flux is zero in the outward direction ($\partial\Omega_3$). The boundary conditions are:

$$T = T_0 \text{ on } \partial\Omega_1$$

$$(-k \nabla T) \cdot \underline{n} = h(T - T_{amb}) \text{ on } \partial\Omega_2$$

$$(-k \nabla T) \cdot \underline{n} = 0 \text{ on } \partial\Omega_3$$

where h denotes the heat transfer coefficient and T_{amb} denotes the ambient temperature. The outward unit normal vector to the boundary surface is denoted by n.

The next step is to multiply both sides of Equation C.3 by a test function ϕ and integrate over the domain Ω. The test function ϕ and the solution T are assumed to belong to Hilbert spaces. A Hilbert space is an infinite-dimensional function space with functions of specific properties. It can be viewed

as a collection of functions with certain nice properties, such that these functions can be conveniently manipulated in the same way as ordinary vectors in a vector space.

$$\int_\Omega k\nabla T \cdot \nabla\phi dV + \int_\Omega (-k\nabla T) \cdot \underline{n}\phi dS = \int_\Omega g\phi dV \tag{C.4}$$

After applying the finite element method on these functions, they are simply converted to ordinary vectors. The finite element method is a systematic way to convert the functions in an infinite dimensional function space to first functions in a finite dimensional function space and then finally ordinary vectors (in a vector space) that are tractable with numerical methods.

The discretization implies looking for an approximate solution to Equation C.4 in a finite-dimensional subspace to the Hilbert space H so that $T \approx T_h$. This implies that the approximate solution is expressed as a linear combination of a set of basis functions ϕ_i that belong to the subspace:

$$\sum_i T_i \int_\Omega k\nabla\psi_i \cdot \nabla\psi_j dV + \sum_i \int_{\partial\Omega} (-kT_i\nabla\psi_i) \cdot \underline{n}\psi_j dS = \int_\Omega g\left(\sum_i T_i\psi_i\right)\psi_j dV \tag{C.5}$$

$$\underline{A}\underline{T_h} = \underline{b} \tag{C.6}$$

where T is the vector of unknowns, $T_h = T_1, .., T_i, ..., T_n$, and A is an nxn matrix containing the coefficients of T_i in each equation j within its components A_{ji}. The right-hand side is a vector of the dimension 1 to n. A is the system matrix, often referred to as the (eliminated) stiffness matrix, harkening back to the finite element method's first application as well as its use in structural mechanics.

Each equation in the system of equations for Equation C.5 for the nodes 1 to n only gets a few nonzero terms from neighboring nodes that share the same element. The system matrix A in Equation C.6 becomes sparse, with nonzero terms only for the matrix components that correspond to overlapping $ij : s$. The solution of the system of algebraic equations gives an approximation of the solution to the PDE. The denser the mesh, the closer the approximate solution gets to the actual solution.

The equations within each element are also known as shape functions. As can be seen in Figure C.1, these functions can be of different order: linear (first-order), quadratic (second-order), and cubic (third-order). Each physics interface has its own unique discretization settings that govern what order shape functions are using for those dependent variables [57]. The default discretization is second-order (quadratic) partially because the PDEs have a dominant second derivative term. If an element is Lagrange it introduces additional nodes (degrees of freedom) within the elements, as can be seen in Figure C.1.

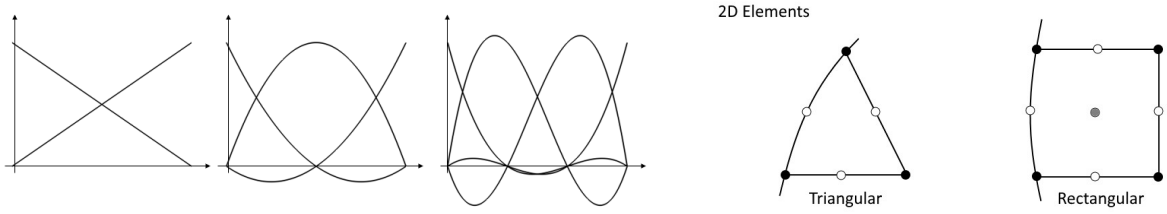

Figure C.1: Linear, quadratic and cubic shape functions within a one-dimensional element (a) and Lagrange elements (b). [57]

D

Details FEM Model

D.1. Geometry
The geometry is shown in Figure D.1 with corresponding values in Table D.1.

D.2. Material properties
For the different material parameters the reader is referred to chapter 3 and Figure D.2.

D.3. Mesh
For the original model the mesh shown in Figure D.3 is used. For scenarios where the cable or geometry is changed physics-controlled meshes with a sufficient fine mesh without errors is used.

D.3.1. Tolerance
The default relative tolerance of the model is 0.01, being the maximum amount of error allowed in your solution. A smaller tolerance gives more accurate results since it includes the maximum deviation that is accepted. Running with a tolerance of 0.001 and 0.00001 give (almost) exactly the same thermal response but more computation time. The default tolerance value of 0.01 is used.

D.4. Run
The model has to be transient to account for environmental differences over time. The model is set to a time stepping of $[1h, 0.5h, 499h]$ to correspond to the measurement period time (steps). Furthermore, the time stepping is set to 'strict' in order for the results to strictly follow the given time stepping. The rest of the conditions are kept in their default settings.

Time stepping is done using the Backward Differentiation Formula (BDF) which is the default setting in COMSOL. As a solver the PARDISO algorithm is used (automatically chosen by COMSOL). By default, shape functions used for the geometry, the temperature in solids (Discretization HT) and the surface radiosity (RAD) are linear Lagrange, quadratic Lagrange and linear respectively (Appendix C).

Table D.1: Geometry parameters.

Description	Value [cm]	axis
Grass height	4	z
Crack length	150	y
Crack width	10	x
Crack height	17	z
Length soil front and back of crack	100	y
Length soil left and right of crack	100	y
Subsoil height	34	z
Cable diameter	0.6	

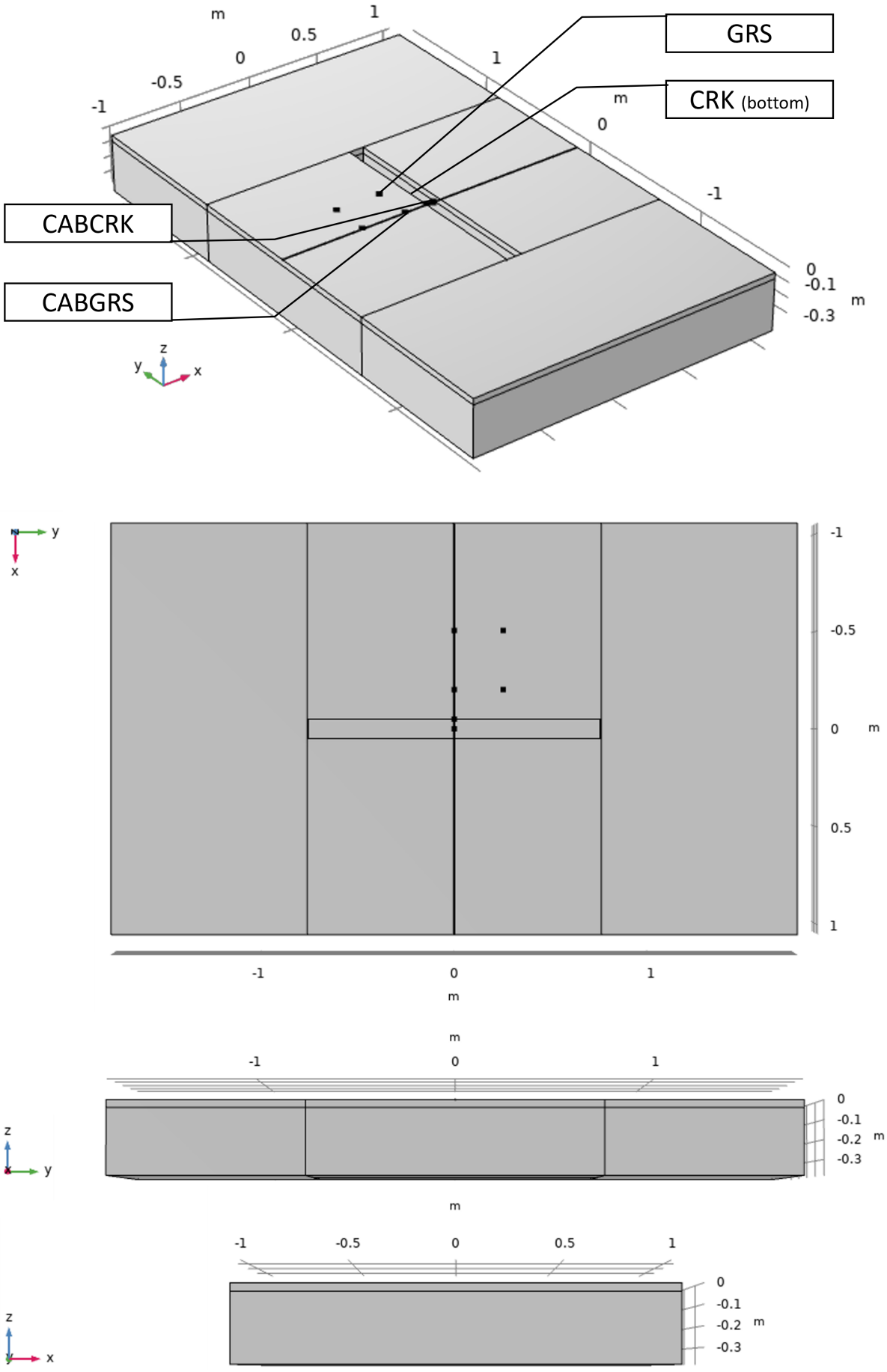

Figure D.1: Geometry FEM model. The points in grass are at a distance of $20cm$ and $50cm$ of the crack middle. x=North, y=West and z=Up.

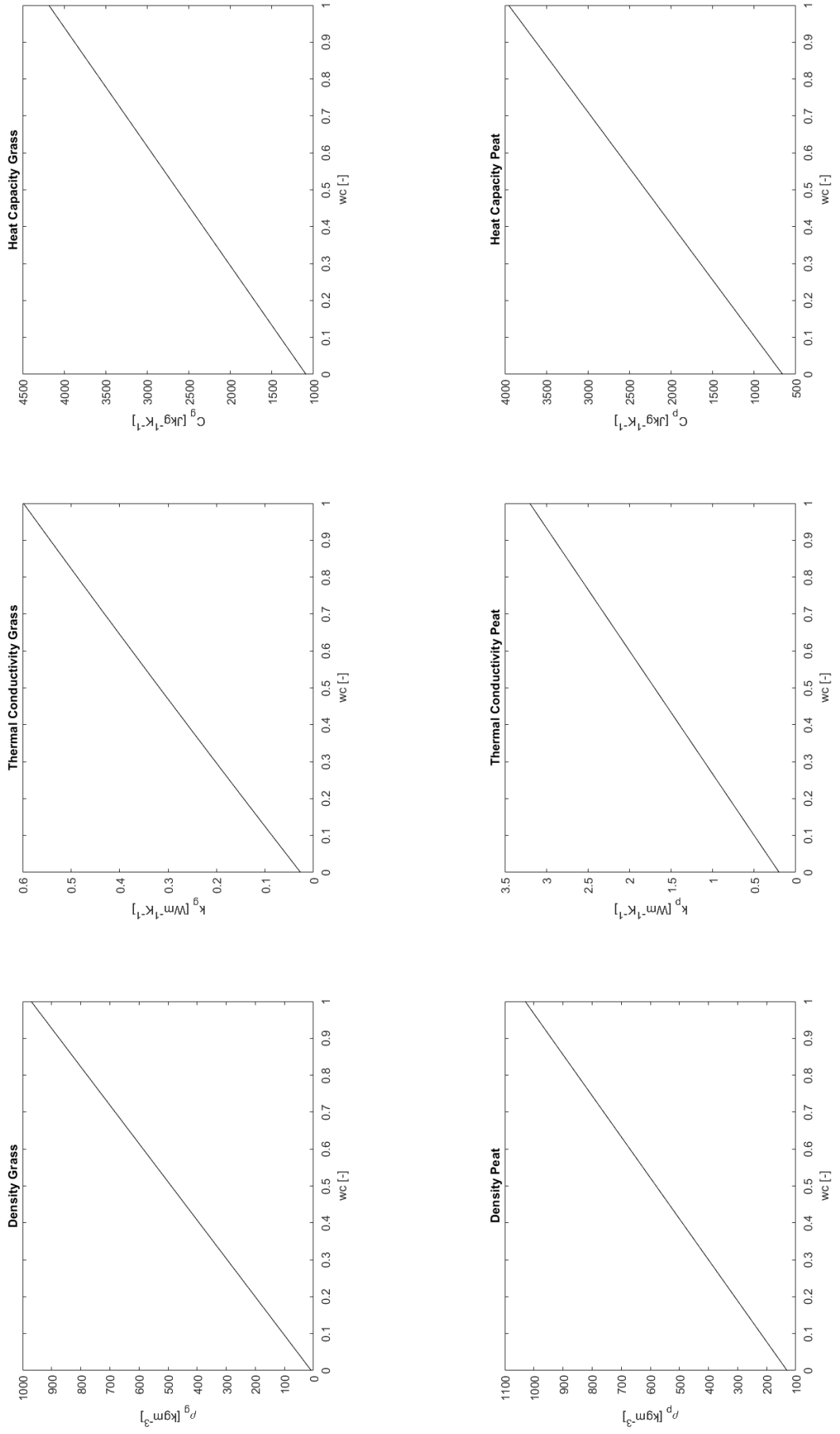

Figure D.2: Water content dependent material properties grass and peat.

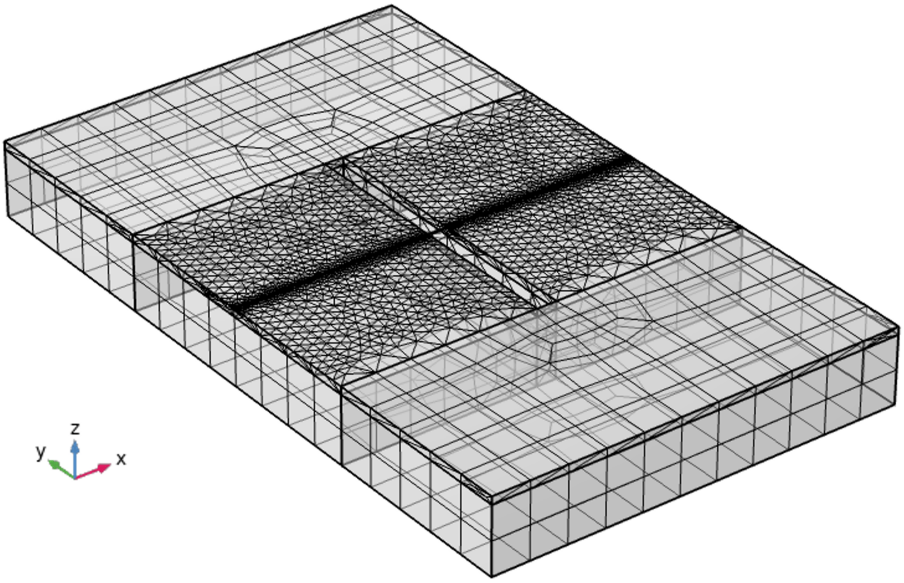

Figure D.3: Mesh FEM model according to section 4.3.

E

Heat Index

The heat index (NL: gevoelstemperatuur) calculated by KNMI is given in Equation E.1. As can be seen in Figure E.1 is the DTS data not equal to the heat index, indicating that the FOS cable is not measuring the heat index temperature.

$$heatindex = c_1 + c_2T + c_3v + c_4T + v + c_5T^2 + c_6v^2 + c_7T^2v + c_8T^2 + c_9T^2v^2 \quad \text{(E.1)}$$

$T[^\circ C] = T_{KNMI}$
$v[\%] = v_{KNMI}$ (humidity)
$[c_{1:9}] = \left[-8.78, 1.61, 2.34, -0.15, 0.012, -0.016, 2.21 \times 10^{-3}, 7.25 \times 10^{-4}, 3.58 \times 10^{-6}\right]$ [58]

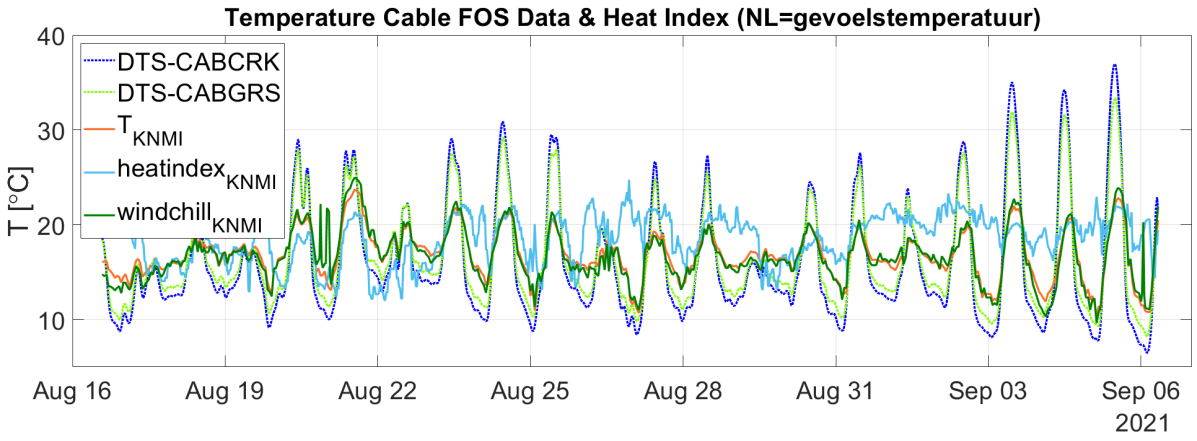

Figure E.1: Heat index KNMI.

F

Influencing Conditions Time Series

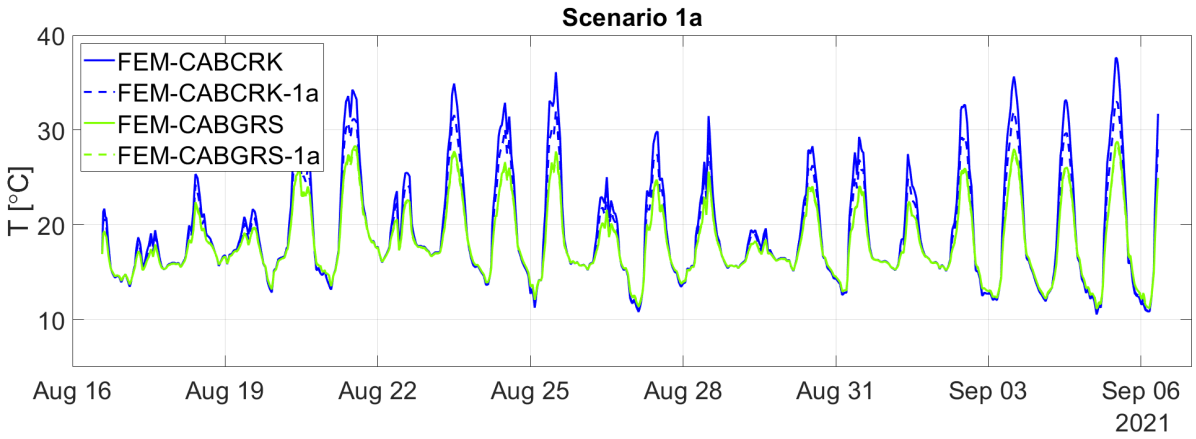

Figure F.1: Scenario 1a: 10 times small crack.

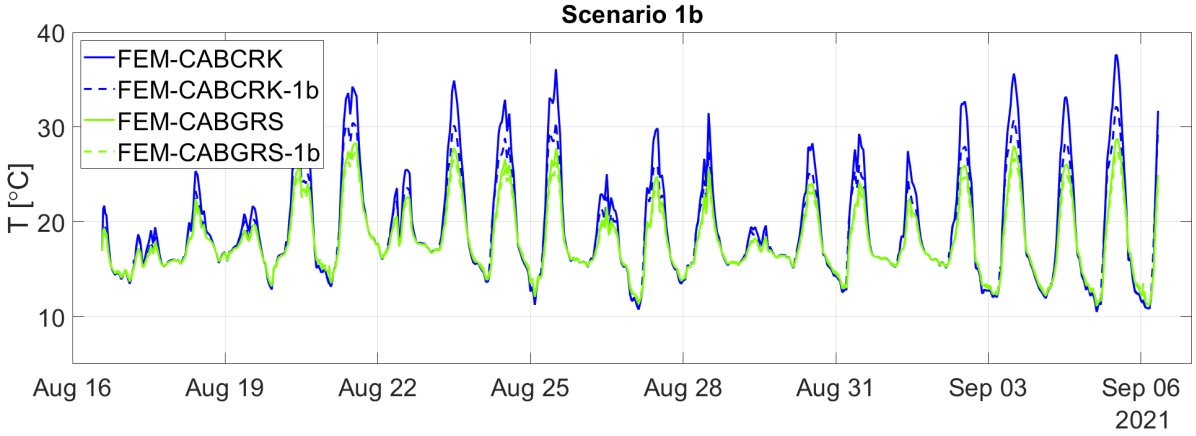

Figure F.2: Scenario 1b: 10 times big crack.

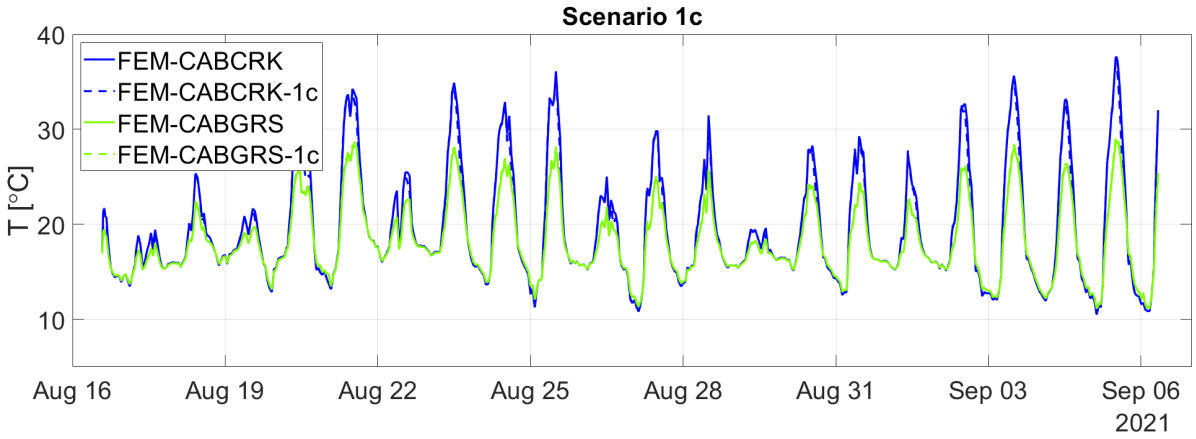

Figure F.3: Scenario 1c: Y-shaped crack.

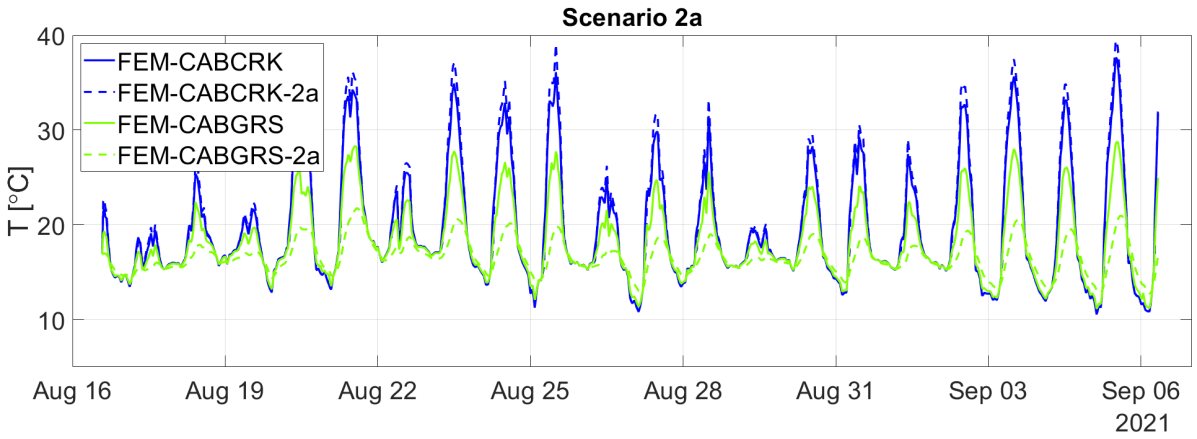

Figure F.4: Scenario 2a: cable below grass canopy.

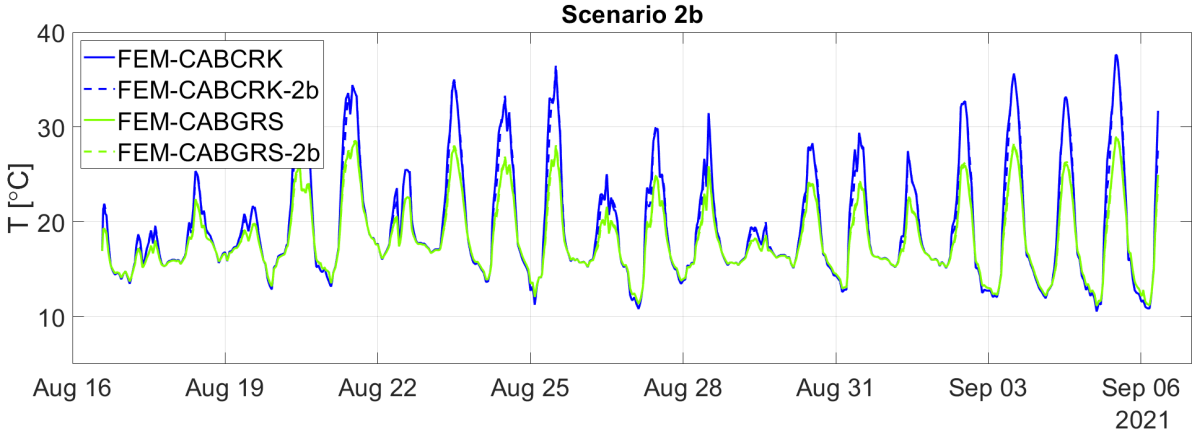

Figure F.5: Scenario 2b: cable diagonal on crack.

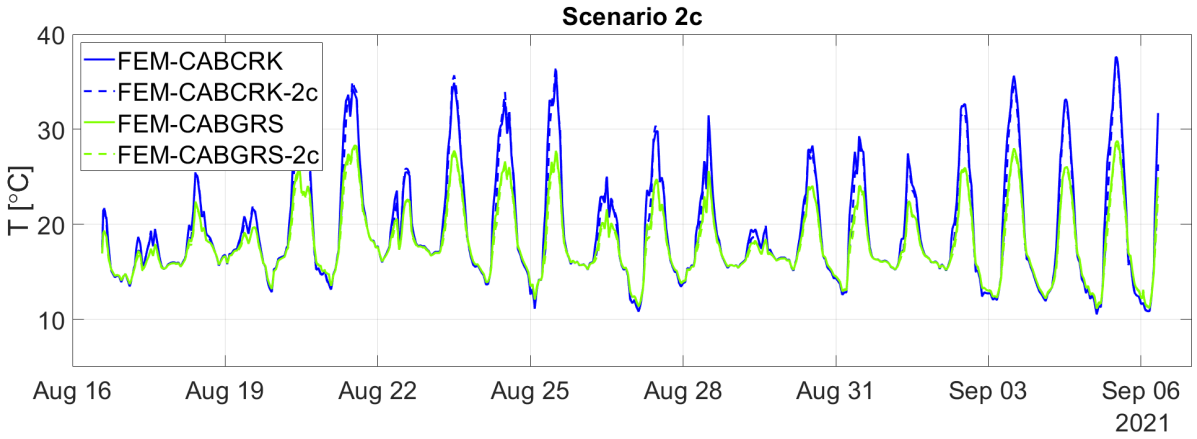

Figure F.6: Scenario 2c: cable parallel on crack.

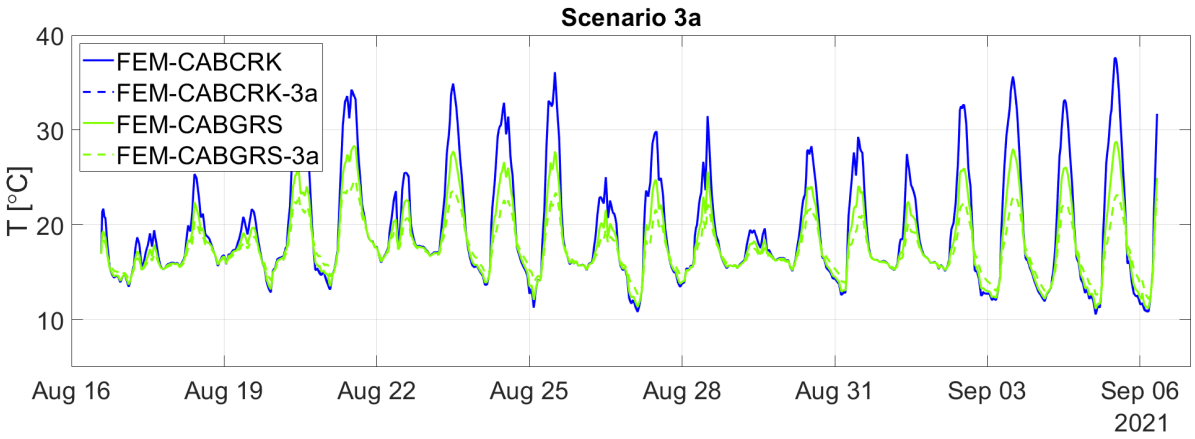

Figure F.7: Scenario 3a: 5 times water content. Dashed line of FEM-CABCRK 3a is below solid line of FEM-CABCRK.

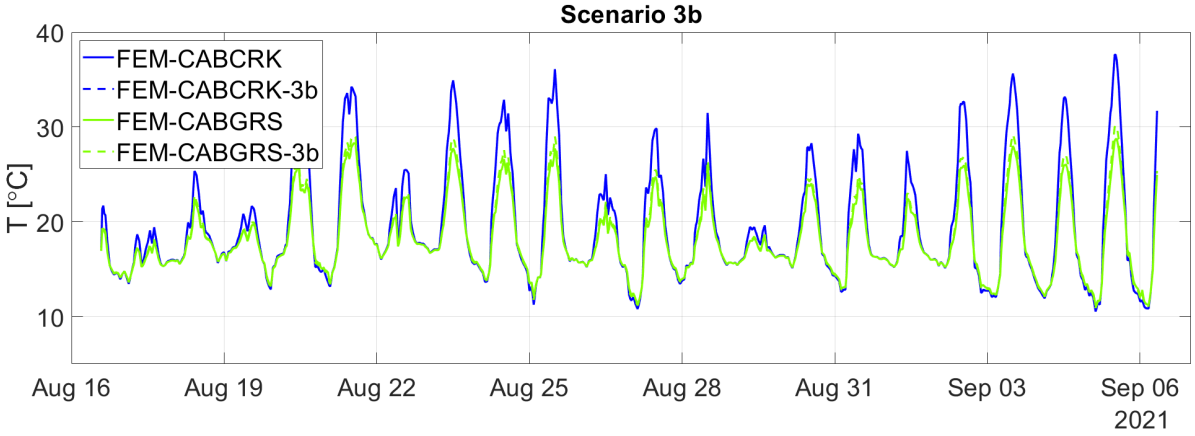

Figure F.8: Scenario 3b: 0.5 times water content. Dashed line of FEM-CABCRK 3b is below solid line of FEM-CABCRK.

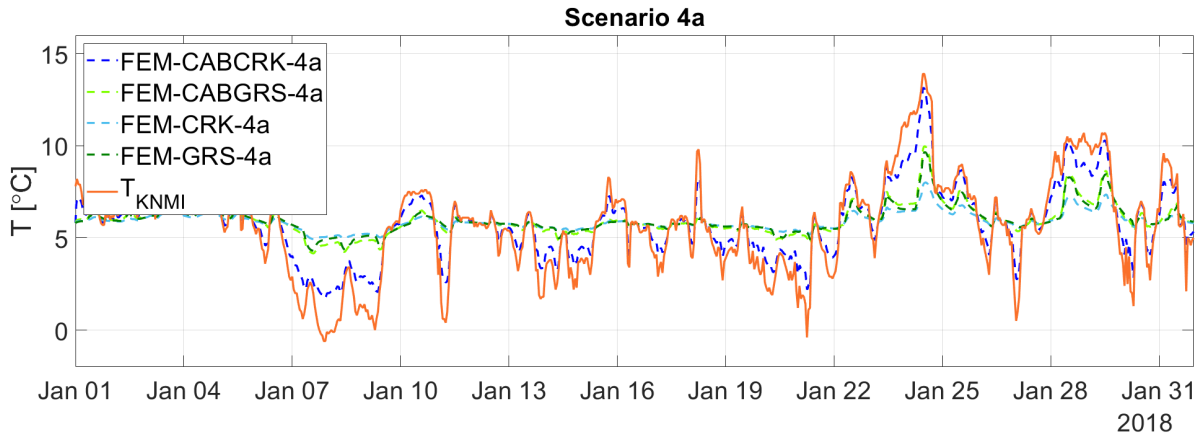

Figure F.9: Scenario 4a: heaviest stormy month (January 2018).

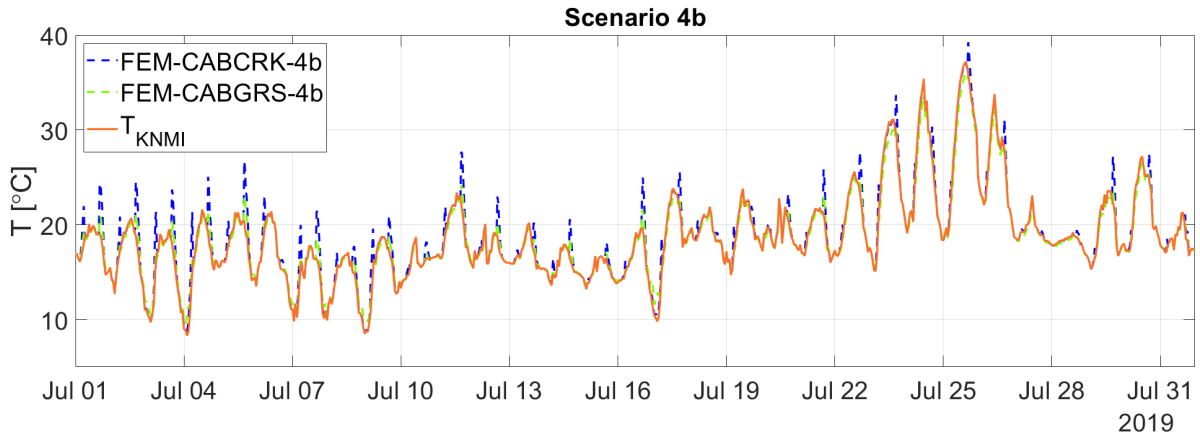

Figure F.10: Scenario 4b: hottest summer (July 2019).

G

Radiation Correction for DTS Information

To find the thermal response of the system, a correction for the radiation overestimation on the cable is desirable. This is done by performing two FEM studies: one including radiation on all exposed surfaces, and one including radiation on all exposed surfaces except the cable. In this way the peat and grass is still heated up by radiation, but the 'extra' heating of the cable is not included. The convection boundary condition is still applied to all exposed surfaces, including the cable. First, the time series without radiation is substracted form the time series including radiation for both FEM-CABCRK and FEM-CABGRS. These differences are then plotted against the corresponding radiation Q_{KNMI} so that a regression plot is formed (Figure G.1) showing the 'over' heating of the cable. This heating (correction) should be subtracted from the measured DTS time series per time step. Cable parts above cracks are warmed up more compared to parts of the cable laid in grass, so cable segments above cracks are more biased than the parts laid in grass. Therefore, to correct the DTS time series, it must be known if the cable segment is in a grass or cracked domain.

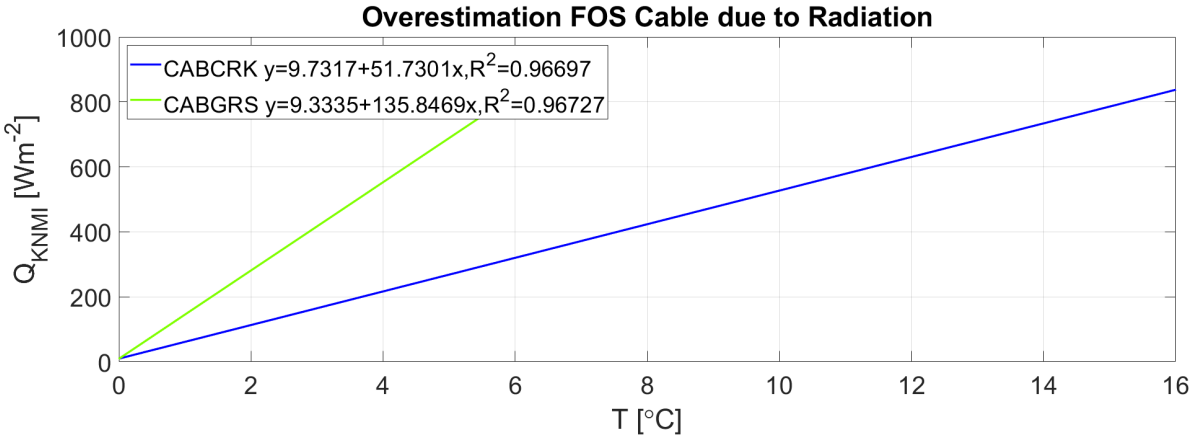

Figure G.1: Radiation correction.